University of Alberta

Construction of a Liquid Scintillation Detector for Relative Megavoltage Dosimetry

by

David Josef Sinn

A thesis submitted to the Faculty of Graduate Studies and Research
in partial fulfillment of the requirements for the degree of

Master of Science
in
Medical Physics

Department of Oncology

Fall 2012
Edmonton, Alberta

Abstract

A radiation detector geared towards megavoltage external beam radiotherapy has been developed using a liquid scintillator and a charge coupled device (CCD). The liquid scintillator used is BetaMax ES (MP Biomedicals, Santa Ana, CA) and the CCD comes from an SPC880NC webcam (Royal Philips Electronics, Netherlands). Simulations and calculations show this scintillator has excellent radiological water equivalence. The detector was also used to measure the relative dose factors, tissue maximum ratios, physical wedge factors, enhanced dynamic wedge factors and modulation factors for a patientint intensity modulated radiotherapy (IMRT) plan. Tests show that the measured values obtained agree well with a Protea ion chamber.

Contents

List of Tables

List of Figures

Chapter 1: Thesis Overview

In modern radiation therapy, precise knowledge of the radiation dose delivered to the patient is of utmost importance. To measure this radiation dose, specialized tools are developed called 'dosimeters.' There are a wide variety of dosimeters that are available commercially, including but not limited to, thermoluminescent devices (TLDs), optically stimulated luminescent detectors (OSLs), ionization chambers, diamond detectors, scintillation detectors and film. Careful selection of the most appropriate detector for the task at hand can be crucial.

Scintillation detectors have a wide variety of applications including use in gamma cameras, computed tomography scanners, high energy physics detection and recently there has been interest in using scintillators for dosimetry of high energy medical linear accelerators (Lacroix, et al., 2008), (Ponisch, et al., 2009), (Frelin, et al., 2008). The motivation for using scintillators comes from the drawbacks inherent in the alternative detection methods. Ion chambers are heavily used for routine quality assurance, but many suffer from not being radiologically water-equivalent and partial volume effects can be troublesome for small intensity modulated radiotherapy (IMRT) fields (Lacroix, et al., 2008). Although the mass energy attenuation coefficient ratio of water and air is relatively constant with respect to photon energy, the restricted stopping power ratio varies, and so energy-dependent correction factors are required for electron beams (Johns

& Cunningham, 1983). Some detectors, such as diodes and metal oxide semiconductor field effect transistors (MOSFETs) show angular dependent response, limiting their reliability and applicability. Diodes are also more negatively affected by radiation damage than scintillators (Beddar, et al., 1992). Diamond detectors offer the advantage of having very low volumes, but show dose rate dependence (Hoban, et al., 1994). The diamond detector normalized current response, i_{norm}, due to dose rate, D_{norm}, can be expressed as:

$$i_{norm} \propto D_{norm}^{\Delta} \tag{1}$$

where Δ a material constant that depends on the equilibrium densities of free electrons and electrons in traps and can be near unity (Hoban, et al., 1994).

Another couple of dosimetry options are TLDs and OSLs, both of which require post-processing and therefore do not give immediate measure of radiation dose.

There have been a few studies of the use of liquid scintillators with medical linear accelerators, but liquids have not been given as much focus as scintillating fibers (Beddar, et al., 2009). One of the concerns regarding the use of scintillators is radiation damage. As the liquid scintillator receives radiation, some of the chemical bonds can become broken and therefore the damaged molecule will not scintillate. Additionally the radiation damage can cause the scintillator to change color, thus decreasing the transmission of scintillation photons through the scintillator (Zhu, 1998). It has been shown that for many scintillators the light output drops linearly with accumulated dose and the reduction can be on the order of 30% for 2 kGy of radiation dose (Hamada, et al., 1999). Although this drop in luminescence is not negligible, the doses delivered in the study were very large relative to the dose that would be measured for quality assurance (<5 Gy). It has also been shown that the radiation damage recovers with time; nearly 95% of the damage may be recovered one month after irradiation.

The main advantage in using a liquid scintillator compared other scintillators is the ease in which phantoms can be created. Plastic scintillators, for instance, need to be carefully machined and handled. On the other hand, liquid scintillators can be poured into a plastic container that is inexpensive to produce and easily machined. Furthermore, if the radiation damage noted above is observed, the pre-existing phantom can simply be refilled with new liquid scintillator as opposed to the case of plastic scintillators, where a whole new phantom would be required. They are also expected to share the tissue equivalence of plastic scintillators (Kirov, et al., 2000).

Scintillation detectors are generally composed of several components: the scintillation material, a light pipe to guide the scintillation photons to the optical detector and optical detector including readout. Historically, photomultiplier tubes have commonly been used to detect the scintillation photons due to their ability to drastically increase the signal without a large increase in random noise (Knoll, 1989). From the viewpoint of this project, photomultiplier tubes have three drawbacks: they require additional electronics to function, they are relatively expensive and two photomultiplier tubes would need for each detector element due to the need to subtract off the Cerenkov signal. Although, in general, all photon detectors require additional electronics, our decision to use a standard webcam charge coupled device (CCD) mitigates this requirement. Photodiodes also need additional electronics such as timing circuits, etc to function and also require multiple diodes per detector unit. The use of CCDs mitigates the aforementioned drawbacks. Firstly, the CCD is intrinsically a matrix of detector elements, meaning that a single CCD can receive several inputs and therefore a second CCD is not needed for Cerenkov subtraction. CCDs can also be purchased as a component of standard commercial webcams, which have all of the necessary electronics included in the package. Because of this fact, CCDs can also be quite readily obtained and easily implemented. This is why we decided to use the CCD; the focus of the project is on the dosimetric properties of the liquid and not on the instrumentation and so instrumentation was sought that would not be overly complex to implement.

The goal of this project is to investigate the dosimetric properties of the liquid scintillator Betamax ES (MP Biomedicals, Santa Ana, CA) using simulation and theoretical analysis as well as to show that an inexpensive CCD can be coupled to the liquid scintillator to produce reasonable dosimetric results. A simple detection system is utilized wherein a plastic fiber optic light guide transports the scintillation photons to a standard webcam CCD that will be connected to a computer for analysis. To the best of our knowledge, the use of liquid scintillator for basic dosimetric measurements in the radiation therapy has not previously been explored.   It is expected that this relatively simple system will work, since a large number of photons produced in the scintillator can be transported to the CCD producing a signal proportional to the energy deposited in the scintillator. One question that remains to be answered is whether or not shot noise levels and the dark current render the system practically usable or not.

Chapter 2: Background

The goal of this chapter is to give the reader all of the background information required to understand the underlying processes involved in scintillator detector operation. It will begin by describing the physics behind the generation of scintillation photons and then describe the process of Cerenkov radiation production. Next, the operation of CCDs will be explained to the extent required for this project. Finally, the motivation and background surrounding each of the experiments will be discussed.

Chapter 3: Materials and Methods

This chapter will take a look at the modeling of the Betamax scintillation cocktail and the various parts comprising the scintillation detector. Included in this section is the methodology behind creating the model used for Betamax, followed by the simulation of various radiological parameters in the EGS Monte Carlo Program. The results of the Monte Carlo simulation are then compared to NIST's ESTAR database (available online) and stopping power calculations from ICRU Report 37.

Following the discussion of the modeling of Betamax, the individual components of the scintillation detector system will be discussed. These include:

- The container that houses the liquid scintillator
- The fiber optic cable that directs scintillation photons towards the detector
- The CCD detector itself
- Shielding used to protect the CCD detector
- USB extension cables and computer used to process the acquired data

- Software used in video acquisition and processing

The methods for performing the dosimetric measurements outlined in Chapter 2 will be discussed last.

Chapter 4: Results

This chapter will present all the experiments performed with the scintillation detector. There will also be a short discussion regarding the accuracy of the measurements taken.

Chapter 5: Conclusions

This chapter will include a discussion of the simulations, calculations and measurements taken and will also discuss the successes and failures of the detector system as a whole. The chapter will conclude by discussing the future work that could be done to improve the detector system.

Chapter 2: Background

2.1 Scintillation

Scintillation can be defined as "luminescence induced by ionizing radiation in transparent, dielectric media. (Lecoq, et al., 2006)" There are several mechanisms through which light can be emitted by a scintillator: fluorescence, phosphorescence and delayed fluorescence (Knoll, 1989). Prompt fluorescence refers to the emission of a photon due to the relaxation of an excited electron. Phosphorescence photons, on the other hand, have longer decay times and also longer wavelength than fluorescence photons because the electrons undergo inter-system crossing to lower energy triplet states before emission of a photon. Delayed fluorescence photons have the same as wavelength as prompt fluorescence photons, but the electron doesn't relax to ground state as quickly. This process doesn't happen immediately because the relaxing electrons initially undergo inter-system crossing to a triplet state and then convert back to the singlet state and fluoresce. In general, a good scintillator will have a large portion of its emitted light in the form of fluorescence and not from other means. The electronic energy levels and radiation induced transitions are shown in Figure 1 for a typical scintillating material.

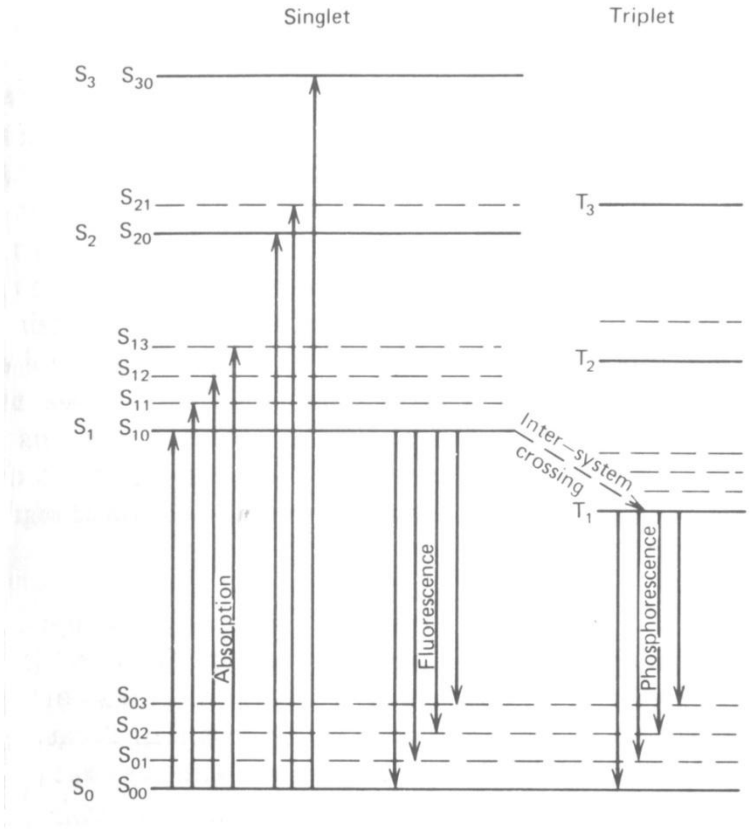

Figure 1: Diagram of excitation and relaxation transitions between energy levels. (From J.B. Birks, 1964)

In Figure 1, the symbols 'S' and 'T' stands for singlet and triplet configurations respectively. The spin 'zero' particles are in the singlet configuration while spin 'one' particles occupy the triplet configuration. The first and second subscripts denotes the electronic energy level and the vibrational energy levels respectively. At standard operating temperatures (around 22°C), almost all of the electrons will be in the S_{00}, or ground state. The majority of electrons are in this state because the difference in vibrational energy levels is much larger than the thermal energy that the electrons possess. As indicated in the figure, when the radiation imparts energy to an electron it can be excited into any one of the higher energy levels. In scintillators, any electrons that are excited to singlet states higher than S_{1x} de-excite to the S_{1x} states by internal conversion on the order of picoseconds (Knoll, 1989). The electrons that are in any of the higher vibrational states quickly transfer their excess energy to neighboring electrons.

There are then two possible processes: emission of a scintillation photon through the fluorescence process, or an inter system crossing to the triplet state. When the electron fluoresces, it can drop into any one of the S_{0x} vibrational states and so the energy of the emitted photon varies. If an electron underwent intersystem crossing after a relatively longer period of time a photon can be emitted through the phosphorescence mechanism. Alternatively, the electron can return to the singlet state and quickly emit a photon through delayed fluorescence.

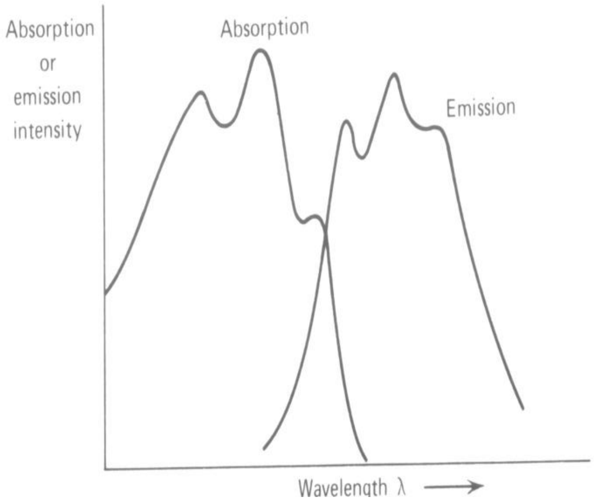

Figure 2: Absorption and emission spectra. (From Knoll, 1989)

It is important for the emission and absorption spectra of the scintillator to be non-overlapping. If the emitted scintillation photons are similar in wavelength to those that are absorbed, the scintillator will have greatly reduced luminescence efficiency due to self absorption. This is typically not a significant problem for scintillators of interest because the radiationless transfers that occur following absorption of energy cause the electron to emit optical photons that the scintillator is transparent to. In the absence of internal conversions, the energy of emitted photons would be the same as the energy required to originally excite the electron and therefore the photon would necessarily have a high probability of causing another excitation. If the emission and absorption spectra are found to have significant overlap, wavelength shifters can be added to push the effective emission spectra towards higher wavelengths. Wavelength shifters are organic chemicals that absorb photons and re-emit them at longer wavelengths (Dai, et al., 2008). By shifting the photons to longer wavelengths, the transparency of the scintillator to its own photons is increased. Furthermore, wavelength shifters are often used to shift the wavelength of scintillation photons to closely match the absorption spectra of the photocathode in photomultiplier tubes.

2.1.1 Liquid Scintillation Cocktails

Liquid scintillation cocktails are composed of one or more solvents and one or more solutes. The solvents make up the vast majority of the volume of a liquid scintillator and have several functions (Howard, 1976). Common solvents include benzene, toluene p-xylene and napthalene. The first function is to allow the solutes to be dissolved within the solvent. The second function is often to allow radioactive samples to be dissolved into the solvent; since this study focuses on external beam irradiation, this is not important for our needs, but it is very important in nuclear medicine. A third function of the solvent is to be the primary acceptor of energy imparted by the radiation. After being excited by ionizing radiation, the solvent particle remains in an excited state for a relatively longer time. This allows efficient energy transfer between the solvent and primary solute, and therefore the ideal solvent will have long decay times and low fluorescence yield so that the primary source of photons are emitted from the solutes.

Scintillator solutes are, as the name would suggest, organic compounds that are dissolved into the solvent. The purpose of the solute is to have the energy imparted from the solvent to be emitted as visible photons. Optimal solutes will therefore have high fluorescence yield, short decay times and a lack of overlap between the emission and absorption spectra (Dyer, 1980). The optimal energy transfer efficiency between solvent and solute depends on the concentration of the solute that needs to be carefully selected. If the concentration is too high or too low, scintillation efficiency drops due to self quenching, yielding reduced signal. Self quenching occurs due to interactions between excited and non-excited solute particles (Horrocks & Wirth, 1968). Often the wavelength of emission from the primary solute is too short to be optimally detected by optical sensors, so secondary solutes are commonly added. These secondary solvents will absorb the short wavelength photons and quickly re-emit them at longer wavelengths.

2.2 Cerenkov Radiation

Cerenkov radiation has been studied since the discovery of radioactivity and has been well covered in the literature (Jelley, 1958). The first recorded observation of Cerenkov emission was by Mme. Curie in 1910, but the "uncanny pale blue light" (Jelley, 1958) was not pursued at that time. The first person to pursue the study of Cerenkov radiation was Mallet, who published his findings between 1926 and 1929. His experiments involved placing various transparent bodies next to radioactive emitters. For all transparent bodies he observed the same continuous spectrum of bluish white photons. This is important to note, as it didn't provide the radiation bands that are consistent with visible photons produced through luminescence. Cerenkov performed a series of experiments from 1934-1939 which were more exhaustive than those performed by Mallet. Cerenkov's experiments showed that the emitted light was due to secondary electrons and not photons as had been previously suspected. Furthermore, he was able to show that the emitted light was emitted with an angular dependence. Around the time that these discoveries were made, Frank and Tamm proposed a theory for the reasoning behind the production of Cerenkov radiation. Cerenkov then devised a series of experiments that characterized the spectrum of emitted photons, the intensity of emitted photons and the dependence on both the index of refraction of the material and electron speed. Research on the topic in the early years was hampered by the lack of sensitive detection equipment, but with the invention of the photomultiplier tube during the Second World War, the interest increased.

Cerenkov radiation is produced when a charged particle moves through a medium. As the particle approaches atoms, they become polarized. If the particle is moving slowly relative to the speed of light, the particle will equally polarize the atoms in all directions and there will be no net electric or magnetic field produced in any direction at a point far from the particle. This situation is illustrated in Figure 3 (a). However, if the particle is moving at a speed that is greater than speed of light in the medium, more atoms will remain polarized behind the charged particle than are polarized ahead of the particle and thus a net field will be produced parallel with the charged particle's track. This is the situation that is presented in Figure 3 (b)

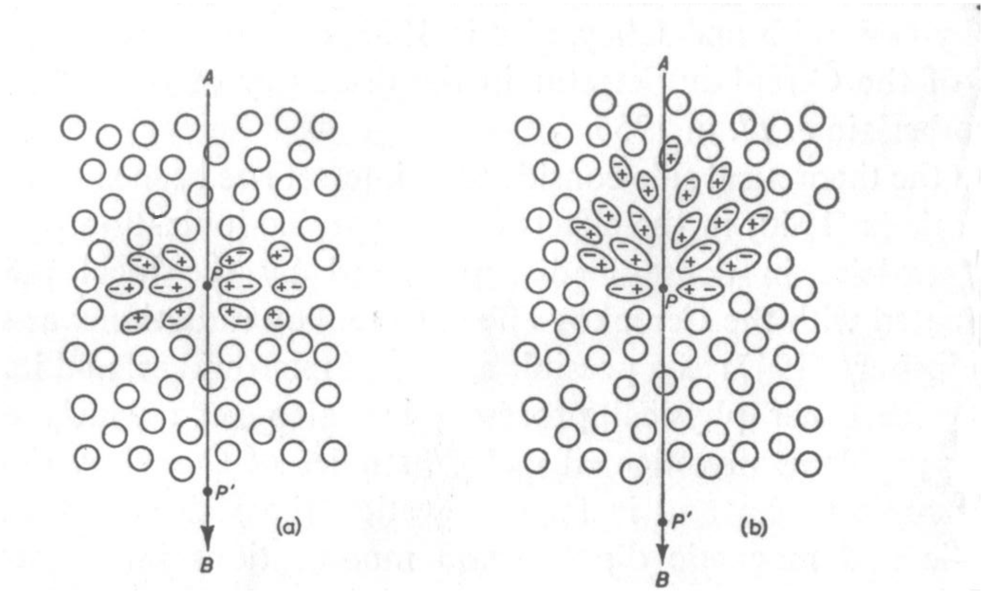

Figure 3: Diagram of polarization of medium due to the presence of a moving charged particle. (From Jelley, 1958)

Due to the net electric field that is created, photons are emitted. There exists a special condition under which the waves emitted along the particle track will constructively interfere, as is illustrated in Figure 4. The figure represents a situation where in the particle is moving from point A to point B. If we define the particle's speed as $v = \beta c$ and the index of refraction of the material to be n, then there exists only one angle for which we see constructive interference. This angle satisfies the following equation, known as the Cerenkov relation (Cerenkov, 1937):

$$cos\theta = {}^{1}/_{\beta n} \tag{2}$$

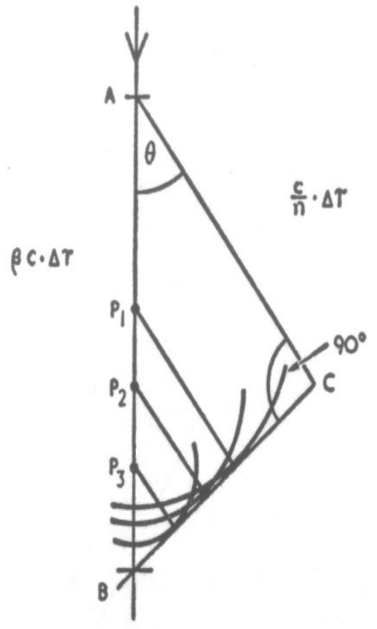

Figure 4: Illustration of the condition leading to constructive interference of the light emitted due to the charged particle motion in the medium. (From Jelley, 1958)

This is very important for our application in that there will be visible photons produced that will be detected but are not directly related to the radiation dose. To detect the scintillation photons, we are using a fiber optic cable that will guide the scintillation photons to the CCD where they will be recorded. Any photons that are produced in the fiber optic (i.e. by Cerenkov radiation) will therefore be measured but they do not indicate the radiation dose that would be deposited at the point of measurement.

The Cerenkov yield for photons of wavelength λ is given by the following equation for a particle with fractional speed β (Charman, 1952):

$$\frac{d^2N}{dl \cdot d\lambda} = \frac{2\pi\alpha}{\lambda^2}\left(1 - \frac{1}{\beta^2 n^2}\right) \tag{3}$$

In the above equation, α is the fine structure constant, roughly equivalent to 1/137, dN/dl is the number of photons emitter per unit path length, λ is the wavelength of emitted radiation, β is the fractional speed of the electron and n is the index of refraction of the material. We can integrate the equation with respect to wavelength and distance travelled to find the number of photons produced in the visible range by a charged particle to be:

$$N = 2\pi\alpha l\left(1 - \frac{1}{\beta^2 n^2}\right) * 1.30 \cdot 10^6 m^{-1} \tag{4}$$

The above formulation assumes a visible range extending from 380-750nm. Using the relativistic energy equation (Tipler & LLewellyn, 2002) we can determine the Cerenkov yield as a function of electron energy as shown in Figure 5. The refractive index used in the data in Figure 5 was 1.492, which is the refractive index of the optical fiber used in the experiment.

To illustrate that Cerenkov radiation is measurable, Figure 6 displays the signal measured by a CCD that arises when our fiber optic light guide is irradiated by several exposures to a 6 MV photon beam of 15·15 cm^2 field size, each exposure delivering 50 MUs at 600 MU/min using a Varian Trilogy accelerator (Varian Medical Systems, Palo Alto, CA). There is no buildup present and there is also no backscatter present: the cable is freely floating in air.

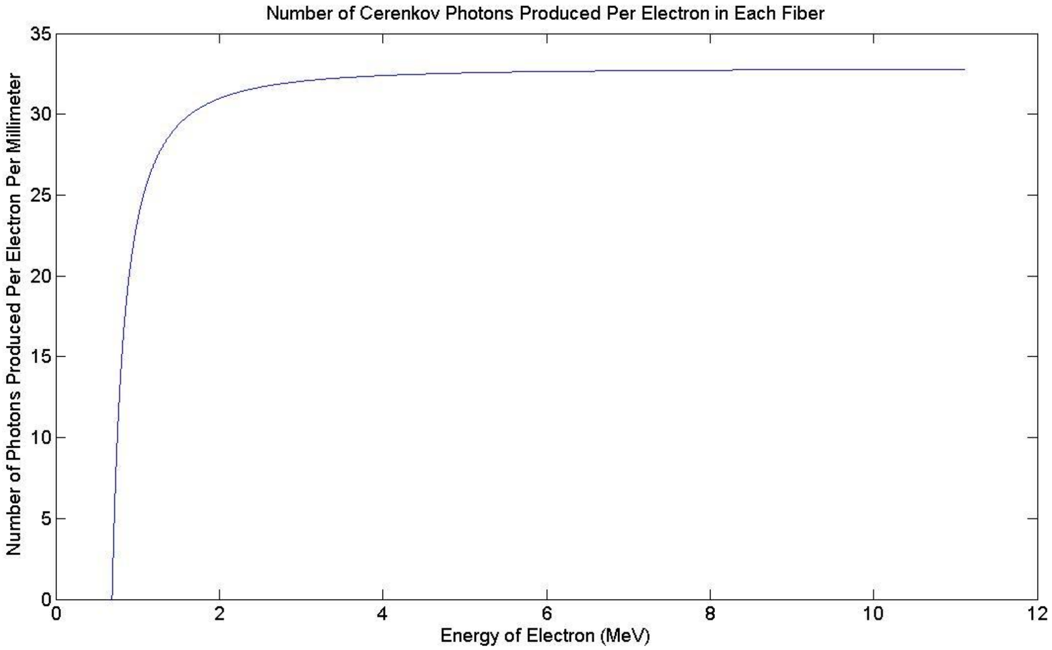

Figure 5: Number of photons produced per electron interacting in the fiber as a function of electron energy

The multiple pulses in Figure 6 occur because the 50 MU field was delivered seven times during the acquisition. The x-axis is displayed in terms of frame number and can be converted to time by dividing the frame number by five, as the acquisition was taken with five frames per second.

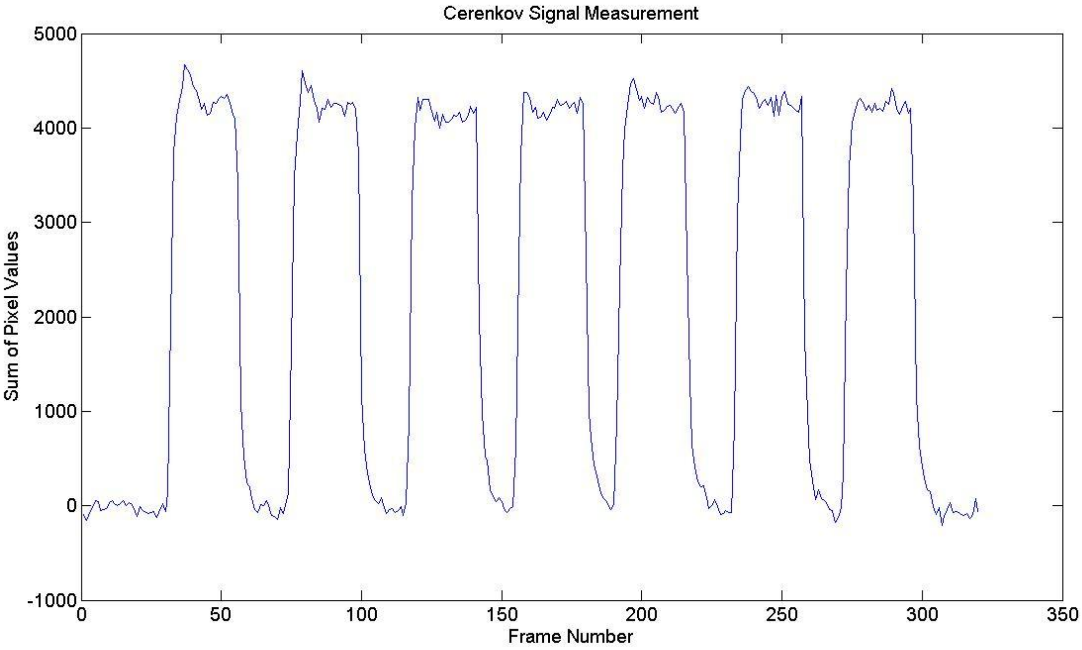

Figure 6: Sample irradiation of an optical fiber illustrating that Cerenkov signal is measureable.

There have been several methods proposed to deal with the problem of Cerenkov radiation confounding scintillation signal (Beddar, 2007). The most notable solutions involve temporal avoidance (Clift, et al., 2002), optical filtration (Clift, et al., 2000) and Cerenkov subtraction via a second reference fiber. The temporal avoidance method requires using a detector with very high temporal resolution, which is not possible with the CCD that was used as our detector. The filtration method involves a fairly complex system of filters and lenses, whereas the dual-fiber method only requires the light from two fibers can be simultaneously read by the optical detector. This approach is well suited for our proposed CCD setup.

Preliminary experiments were also conducted to determine the relative importance of the Cerenkov signal in the standard irradiation conditions of our experiments. Figure 7 shows a standard irradiation procedure where 12 sequential irradiations were measured with the CCD. The dose rate was 600 MU/min with the scintillator placed at a source-to-axis (SAD) of 100 cm , having 2.5 cm of solid water buildup and 11.5 cm of backscatter. Each irradiation delivered a total of 50 MUs with a 10x10 cm^2 field using a 6 MV photon beam. In the example above, the mean signal measured through the reference fiber (i.e. the Cerenkov signal) was 5.37% of the mean scintillation signal. The above example makes it clear that the detection of Cerenkov photons will provide a non-negligible contribution to the signal and needs to be dealt with accordingly.

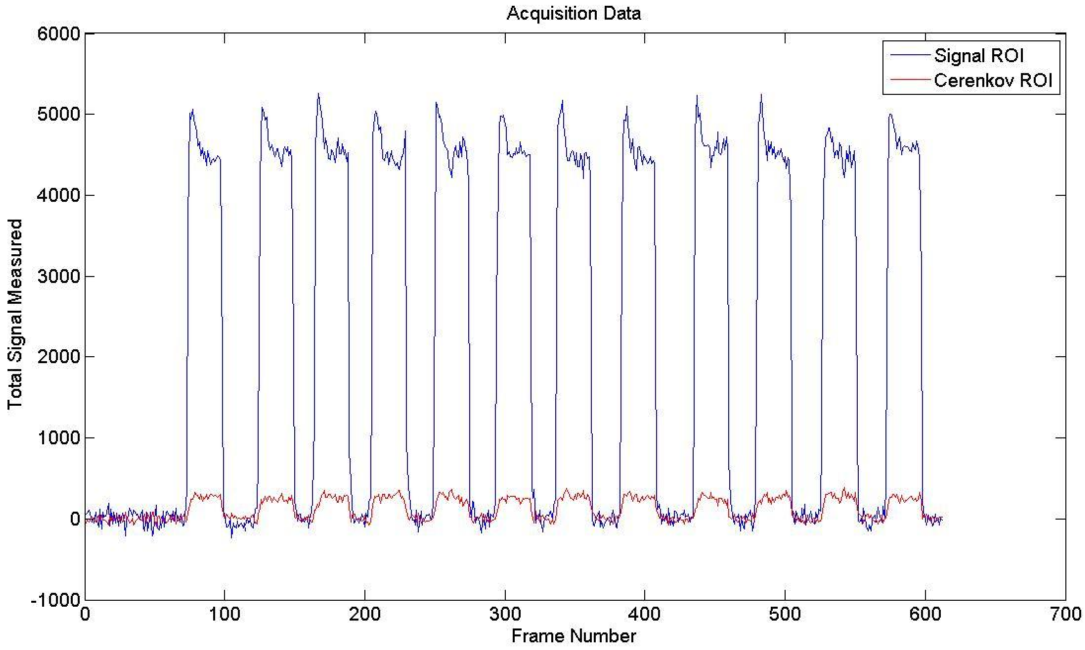

Figure 7: Plot showing the simultaneously measured signals from the liquid scintillation material and a bare, reference optical fiber (i.e. Cerenkov only)

2.3 Charge Coupled Devices

Charge coupled devices, or CCDs, were invented by Boyle and Smith at Bell Telephone Laboratories in 1969 (Janesick, 2001). The CCD technology has been extensively developed ever since and the CCDs have become a mainstay of scientific imaging (Magnan, 2003). The use of CCDs in image acquisition is motivated mainly due to the low noise characteristics, wide spectral detection range, high quantum efficiency (Howell, 2000) and nearly perfect linearity (Martinez & Klotz, 1998). A CCD is essentially a matrix of individual silicon detector elements that are read out sequentially to create an image. A popular way to visualize the sequential reading of the elements is to think about buckets on conveyer belts in a rainstorm, as in Figure 8 below. The rain can be likened to the visible photons that interact with the buckets, which represent the pixels. After the rain has stopped, the buckets on the right hand conveyor belts are moved to the left and the buckets on the left conveyer belt are moved downwards towards the graduated cylinder. By sequentially measuring the amount of rain in each bucket we can know how much rain fell on each position where a bucket was originally located. In this manner, we can pass the charge collected in each pixel towards a measurement device to determine the amount of charge that was generated in each pixel. A more detailed description follows.

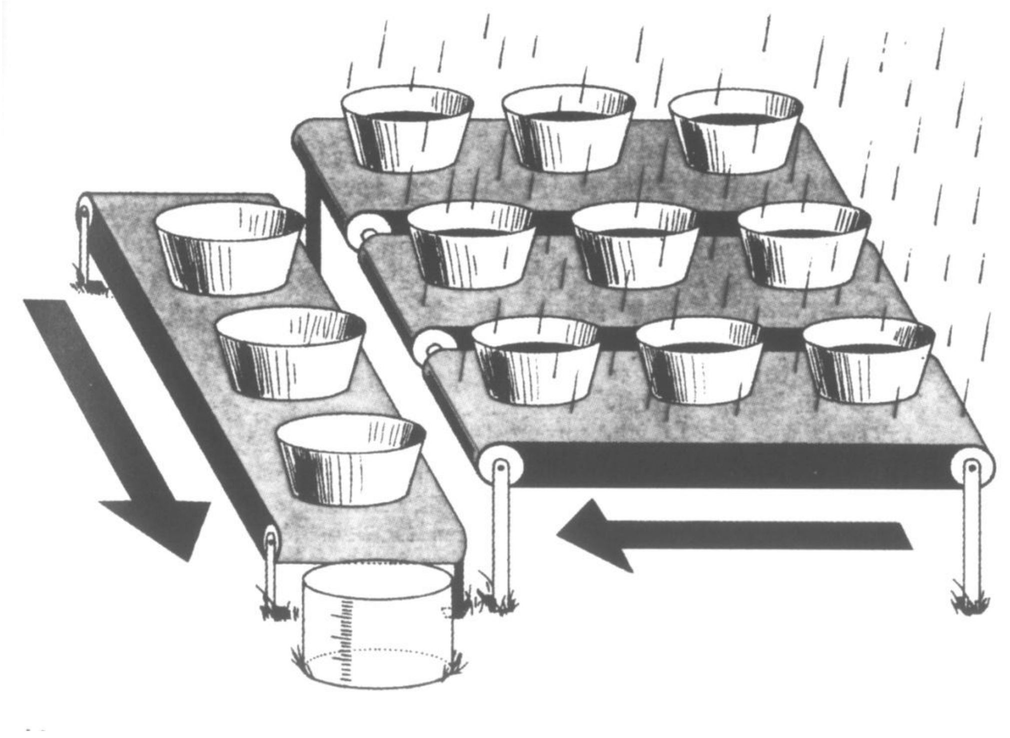

Figure 8: diagram displaying how individual CCD pixels are read. (From Janesick, 1987)

When photons in the optical range impinge upon one of the pixels, a photon can excite one of the silicon electrons from the valence band to the conduction band. To prevent the electron from de-exciting back into the valence band, an electronic potential is applied. The potential is supplied by a series of cathodes called gates.   At the end of the specified exposure time, the voltages are manipulated so that the collected electrons are held in the +10 volt potential well. Simultaneously, the zero volt gate then changes to +10 volts, the gate that previously had a +10 volt potential changes to +5 volts and the gate that had a +5 volt potential changes to zero volts . This forces the electrons to migrate to the deeper potential well and correspondingly forces them to change their location in a specific direction. This is shown in Figure 9 below (Walker, 1987).

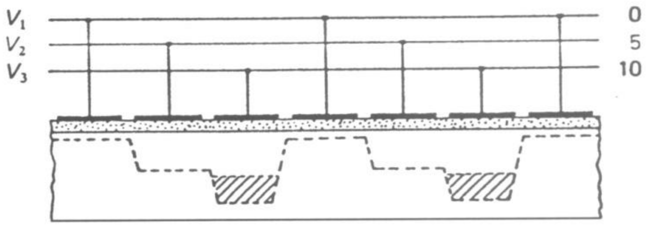

End of exposure

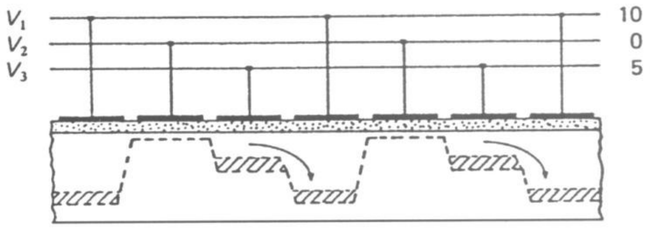

Charge transfer

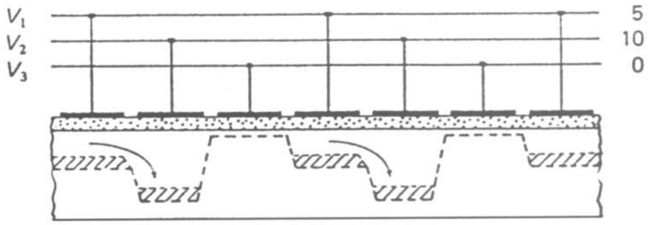

Figure 9: Diagram of charge transfer through gate voltage modulation. From Walker (1987)

The columns of pixels move simultaneously through the rows. The final row is shielded from right and is called the output register. Once in the output register, the pixels are read in one at a time and sent to output electronics. The CCD can have multiple rows of pixels in the output register to enable less processing time required between frames and some CCDs even have an output register that is the exact same size as the imaging part of the CCD to avoid any delays in processing.

After the voltage has been read, an analog to digital converter converts the signal into a digital value to be analyzed.

2.4 Beam Characterization Measurements

2.4.1 Relative Dose Factor

The Relative Dose Factor (RDF) is defined as "the dose rate at a reference depth for a given field size 'r' divided by the dose rate at the same point and depth for the reference field size" (Khan, 1994) and is sometimes referred to as the Total Scatter Factor. The RDF is the product of two factors, the Phantom Scatter Factor and the Collimator Scatter Factor.

As the collimator jaws are opened wider there is increased scatter radiation from within the linear accelerator (linac) head that contributes to the primary beam. The Collimator Scatter Factor accounts for this increase in the dose rate as a function of field size. To measure the Collimator Scatter Factor, one can measure the dose rate in air for varying field sizes with an ionization chamber with the following caveats:

- The ion chamber must have a build up cap that will provide transient charged particle equilibrium yet will have negligible scatter produced with the build up cap
- The ion chamber and build up cap need to be completely covered by the beam for all field sizes
- The ion chamber is placed at 100 cm SAD, which coincides with the isocenter of the linear accelerator

The Phantom Scatter Factor accounts for increased scattered radiation produced in the phantom with increasing field size. This factor should be measured at the depth of maximum dose and is not typically measured directly, as this measurement would require introducing additional field collimation at the surface of the phantom to remove scatter from the linear accelerator head.

The Relative Dose Factor and Head Scatter Factor are measured initially at the time of commissioning a new radiothereapy linear accelerator and measurements are repeated on an annual basis(Klein, et al., 2009).

2.4.2 Tissue Maximum Ratio

The Tissue Phantom Ratio relates the doses of two points that have the same SAD, generally 100 cm, but are located at different depths in the phantom. The Tissue Maximum Ratio (TMR) is a special case of the Tissue Phantom Ratio but with the reference point being the depth of maximum dose. This factor is used in reference to doses in water.

TG-142 recommends that the TMR be measured on an annual basis at a 20 cm depth relative to a 10 cm depth and require that the result agrees to within 1% of baseline measurements.

2.4.3 Physical Wedge Factor

Historically, beam profiles were often modified by inserting a physical wedge filter into the beam (Khan, 1994). These wedges are made of very dense materials such as lead, cerrobend or steel. By inserting one of these wedges into the field, one can produce a gradient in the beam that will produce curved isodoses. These fields are primarily used for compensating the depth dependent gradient of two beams that are oriented perpendicular to each other in a treatment plan.

The wedge factor is defined as:

$$WF = \frac{D_{blocked}}{D_{open\ field}} \tag{5}$$

and is measured at a reference depth beyond the depth of maximum dose (d_{max}) along the central axis of the beam. 'D' in the above formula is the absorbed dose. It is recommended that wedge factors are measured on an annual basis for each beam energy, every wedge angle and for a number of representative field sizes (Klein, et al., 2009). At the Cross Cancer Institute, where this work was carried out, we have 15°, 30°, 45° and 60° physical wedges. It is additionally recommended that wedge placement accuracy is measured on a monthly basis. This is to ensure that when the wedge is inserted into the linac's interface mount at its seated position. This is evaluated by measuring the wedge factor in both the 'in' (thin edge of wedge facing the gantry) and 'out' (thin edge of wedge facing away from the gantry) orientations.

2.4.4 Enhanced Dynamic Wedge Factor

Enhanced dynamic wedges (EDW's) are functionally similar to physical wedges in that the beam profile is altered, but EDW's do not use a physical filter. Instead, one collimator jaw is swept through the field in a computer-controlled motion to generate the desired dose distribution. The delivery is a two-stage process beginning with an irradiation using an open field followed by an irradiation with jaw motion (Leavitt, et al., 1990). The computer references segmented treatment tables to determine how fast the jaw should move to obtain the desired wedge angle (Liu, et al., 1998).

It is recommended that the wedge factors for all energies are measured on a monthly basis because very small changes in jaw position can change the wedge angle (Klein, et al., 2009).

2.4.5 Inverse Square

The intensity of radiation produced from a point source varies proportionally to the inverse square of the distance between the source and measurement point. This is simply due to the fact that for any spherical shell drawn around the source the total amount of radiation passing through the shell is constant. As larger shells are drawn, the surface area increases proportionally to the square of the shell's radius and so the amount of radiation per unit area decreases proportionally to the square of the radius.

One can therefore relate the dose in air to point 'A' to the dose in air to point 'B' by the simple relationship:

$$IS = \left(\frac{r_A}{r_B}\right)^2 \tag{6}$$

By varying the source to detector distance, we can vary the dose rate. We can therefore verify the claim that the response from liquid scintillators is independent of dose rate by taking sequential measurements with increasing source to detector distance and ensuring that the detector response varies as predicted by the above response.

Unfortunately, when detecting radiation from a linear accelerator, the inverse square relationship does not strictly hold true. The first reason for this is that the focal spot of a linear accelerators photon generation is not infinitesimally small. Because of this, the relationship will break down for small source to surface distances (SSD's). Another reason is that the inverse square only applies to the primary beam and hence does not account for variations in the scattered radiation. These two factors will contribute to discrepancies at both low and high SSD's.

2.4.6 Intensity Modulated Radiation Therapy

Intensity Modulated Radiation Therapy (IMRT) has given clinicians the ability to deliver highly conformal treatments with ionizing radiation. IMRT, as it is essentially the mainstream method today, was first envisioned in 1992 (Convery & Rosenbloom, 1992) and implemented clinically in 1996 (Carol, et al., 1996). Since that time, significant research has been done and many advancements have been made and, as such, IMRT is widely used today (Bortfeld, 2006).

Chapter 3: Materials and Methods

3.1 Modeling of Betamax ES

The Betamax ES liquid scintillation cocktail is produced by MP Biomedicals (MP Biomedical, Santa Ana, CA). The two solvents used in Betamax are approximately 50% alkylate 225 (Alk-225) and 50% phenyl xylylethane (PXE) (personal communication, Ted Hardman of MP Biomedicals). Due to the exact chemical composition being proprietary information, only given approximate concentrations were given, even when a non-disclosure agreement was offered. MP Biomedicals has provided us with technical reports and MSDS data for both of the aforementioned chemicals, allowing us to gather information on their properties.

There are also two solutes that are used in Betamax, and these are PPO and Bis MSB. PPO is a primary solute with a concentration of 6.6 g/l of Betamax. PPO is widely used as a primary solute (Dyer, 1980). A graphical representation of the molecular structure was produced (see Figure 10) using a freeware program called WinDrawChem, which is available for download online at www.xdrawchem.sourceforge.net/windrawchem. All further chemical structure images in this section are produced using this program

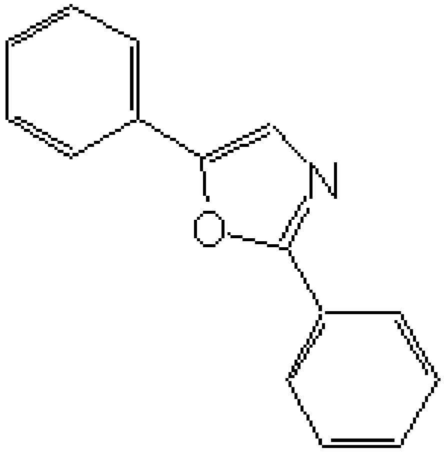

Figure 10: Schema of the chemical structure of PPO

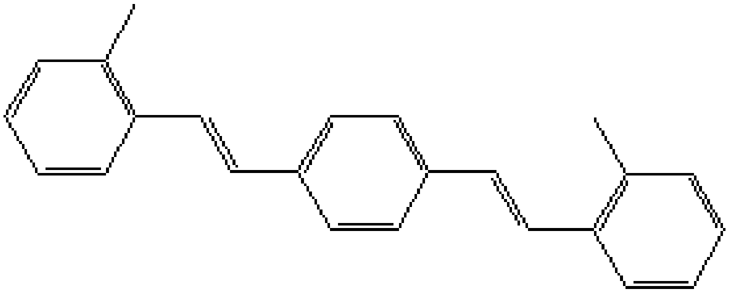

Figure 11: Schema of the chemical structure of Bis MSB

The secondary solute used in Betamax is Bis MSB with a concentration of 0.092 g/l of Betamax (see Figure 11). Bis MSB is commonly used as a secondary solute because it is less susceptible to quench effects than other secondary solutes

(Dyer, 1980). Quench effects are defined as any deposition of energy in the medium that does not lead to the emission of fluorescence photons. Neither of these two solutes is included in the Betamax model due to their extremely low concentrations.

Alkylate 225 (see Figure 12) is a chemical comprised of a benzene group with an attached variable-length chain of CH_2 groups, capped by a CH_3 group. MP Biomedicals has provided a document that details the composition of the Alk-225 that was used in Betamax, which tells us that the average molecular weight of Alk-225 is 243.83 g/mol. Given that the molecular formula for Alk-225 is $C_6H_5{\cdot}C_nH_{2n}{\cdot}CH_3$, one can determine that the average chain is 10.8 carbons long. This can be done as follows:

$$m_{Net} = (7+n)m_C + (8+2n)m_H \tag{7}$$

$$n = \frac{m_{Net} - 7m_C - 8m_H}{m_C + 2m_H} \tag{8}$$

Using values of m_{Net}=243 g/mol, m_C=12.011 g/mol and m_H=1.00 8 g/mol one gets n=10.8. Note that, of course, the chain length depicted in Figure 12 is not the correct chain length and is shown for illustrative purposes only.

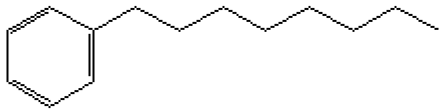

Figure 12: Schema of the chemical structure of alkylate 225

Phenyl xylylethane is similar to Alk-225 in that it is comprised of benzene rings and extra carbon and hydrogen attachments, but instead of a single benzene ring, PXE has a dual benzene structure. We have been supplied by the manufacturer with an MSDS sheet and the molecular weight was obtained online to be 210.31 g/mol. The chemical formula for PXE is $C_{16}H_{18}$, and a diagram of the molecular structure is shown below in Figure 13.

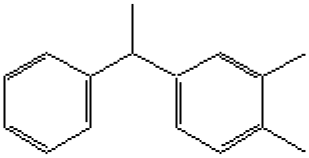

Figure 13: Schema of the chemical structure of phenyl xyxlyl ethane

The preceding two chemicals were used in the computer model for the radiological properties of Betamax and the specifics on all parameters used in the modeling are discussed in Section 3.3.

3.2 Theoretical Background for Stopping Power Ratio Calculation

All of the computer simulations were performed with the EGSnrcMP program, which closely follows the formalism established in ICRU report number 37. ICRU 37 outlines the methods to calculate the stopping powers for electrons and positrons in matter. The dosimetric properties for Betamax had to be determined for each of the constituent compounds first, and then summed in a linear combination to obtain the gross properties of the entire cocktail. The following section will outline how we determined the restricted mass collision stopping powers for any given compound. The equation for the restricted mass collision stopping power is given as:

$$\frac{L}{\rho} = \frac{2\pi r_e^2 mc^2}{u}\frac{1}{\beta^2}\frac{Z}{A}\left[ln^2\left(\frac{T}{I}\right) + \ln\left(1 + \frac{\tau}{2}\right) + G^{\pm}(\tau,\eta) - \delta\right] \quad (9)$$

In the above equation, L is the restricted stopping power, ρ is the density of the substance, r_e is the classical electron radius, u is the atomic unit, T is the electron or positron's kinetic energy and I is the ionization potential of the target medium. Furthermore:

$$\tau = \frac{T}{mc^2} \ and \ \eta = \frac{\Delta}{T} \quad (10)$$

Δ is the fractional threshold energy, i.e.) all hard and soft collisions involve energy loss less than this threshold are accounted in the restricted stopping power while energy losses larger than the threshold are part of hard delta-rays. The G term arises due to the introduction of Moller and Bhabha scattering (for electrons and positrons respectively) into the Bethe-Bloch equation and is given by:

$$G = 1 - 2\beta^2 + \ln\left(4\eta(1-\eta) + (1-\eta)^{-1} + (1-\beta^2)\left[\frac{\tau^2\eta^2}{2} + (2\tau + 1)\ln(1-\eta)\right]\right) \quad (11)$$

The δ term is the density effect parameter and is given as:

$$\delta = \sum_{n=1}^{N} f_n \ln\left[1 + \frac{\hbar^2 l^2}{E_{nL}^2}\right] - \left(\frac{1}{\omega_p}\right)^2 (1 - \beta^2) \quad (12)$$

f_n is the fraction of electrons inhabiting the n^{th} orbital, ω_p is the plasma frequency and E_{nL} are the energy levels of the longitudinal oscillators. The plasma frequency is defined as:

$$\omega_p = \sqrt{\frac{4\pi e^2 n_e}{m}} \tag{13}$$

n_e is the total number of electrons per unit volume. The plasma frequency describes the frequency of oscillations in the electron density. To obtain the value of l in equation 12 above one must solve the following equation for l:

$$\beta^{-2} - 1 = \hbar^2 \omega_p^2 \sum_{n=1}^{N} \frac{f_n}{E_{nT}^2 + \hbar^2 l^2} \tag{14}$$

E_{nT} is the n^{th} energy level of a transverse oscillator. The E_{nL} and E_{nT} levels - are approximated as:

$$E_{nT} = \mu_{ST} E_n \; and \; E_{nL} = \sqrt{\mu_{ST}^2 E_n^2 + f_n \hbar^2 \omega_p^2} \tag{15}$$

E_n is the energy of an electron in the n^{th} orbital of the target medium and μ_{ST} is the Sternheimer factor, which can be determined by solving the following equation:

$$\sum_{n=1}^{N} f_n \ln\left[\sqrt{\mu_{ST}^2 E_n^2 + f_n \hbar^2 \omega_p^2}\right] = \ln(I) \tag{16}$$

First of all, the mean excitation energies of the compounds in the solvents must be determined. To do so, the Bragg Additivity rule was used. The Bragg Additivity rule is given as follows:

$$\ln(I) = \frac{\sum w_j \left({Z_j}/{A_j} \right) \ln(I_j)}{\sum w_j \left({Z_j}/{A_j} \right)} \tag{17}$$

In the above equation, one needs to sum over all of the atomic species that make up the compound and w_j is the fraction by weight of the j^{th} atomic component. Once the mean ionization energy has been determined, one can proceed to solve equation 16 for the Sternheimer factor. This then allows one to isolate equation 14 for l and its value is substituted into equation 12 for the final determination of the density effect parameter.

3.3 Numerical Evaluation

The following table summarizes some of the basic properties of both alkylate 225 and PXE. In the table, n_C, n_H and $n_{electrons}$ are the number of carbon atoms, hydrogen atoms and the number of electrons per molecule of the compound respectively.

Name	Fraction by Weight	Molar Mass (g/mol)	n_C	n_H	$n_{electrons}$
Alkylate 225	0.50	243.84	17.8	29.8	136.6
PXE	0.50	210.32	16	18	114

Table 1: Some basic properties of the chemicals comprising Betamax

These values are used in equation 17 alongside the mean excitation energies of the elements to calculate the mean excitation energies of the compounds.

Name	Z	A	Z/A	Mean Excitation Energy (eV)
Alkylate 225	136.6	243.83	0.560	59.17
PXE	114	210.32	0.542	64.53

Table 2: Calculation of the mean excitation energy for the constituents of Betamax

The various atomic energy levels and the number of electrons in each orbital is determined so that equations 14, 16 and 17 can be numerically evaluated. The fraction of electrons in the n^th orbital, $f_{n,}$, is then calculated and the resulting values are compiled in table 3. Table 4 provides the shell identification and shell energy corresponding to four energy levels for the f_n values given in table 3. The energy levels of the shells were obtained by Carlson (Carlson, 1975). There are more recent sources for the energy levels, but the values from Carlson were used so that the results would match those obtained in ICRU 37.

Name	f_i	f_2	f_3	f_4
Alkylate 225	0.2182	0.2606	0.2606	0.2606
PXE	0.1579	0.2807	0.2807	0.2807

Table 3: Fraction of electrons contained in each subshell

Energy Level	**Corresponding Shell**	**Energy (eV)**
1	H K	13.60
2	C K	288
3	C L_1	16.59
4	C L_2	11.26

Table 4: Identification of shells/subshells and their corresponding energies

A number of Matlab (version R2009b, Mathworks, Natick, MA) programs were written to solve the above systems of equations in reverse order. Once the mean excitation energies have been determined, the Sternheimer factor can be solved for using equation 16. The Sternheimer factor is commonly in the range of 1-2 for most realistic compounds. Having the value for the Sternheimer Factor allows us to solve for the value of *l* in equation 14. Having determined *l*, equation 12 can be used to solve f or the density effect parameter. The results were then combined as a linear combination of the constituent's composition by weight to get the overall density effect parameter.

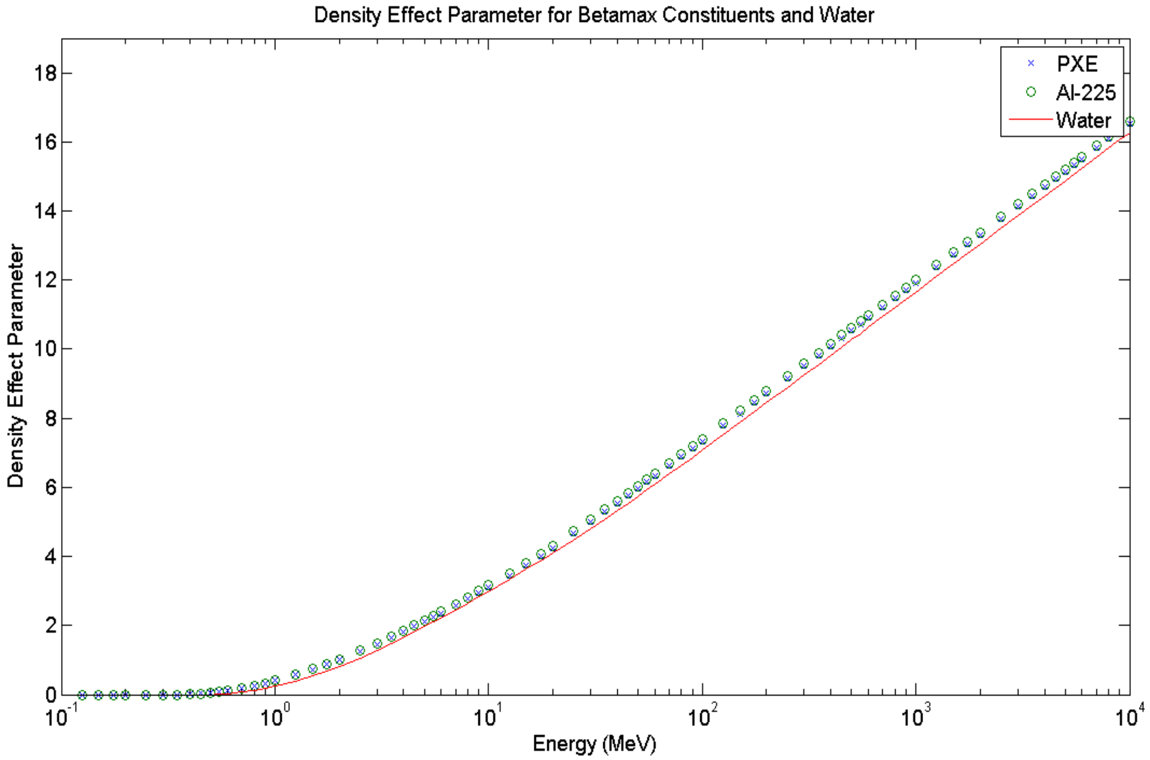

Figure 14: Calculation of density effect parameter for Betamax's constituents and its comparison with water

There is a minimum kinetic energy of the particle for which the density effect formalism applies. The minimum particle speed, β_o, is given by:

$$\beta_0^2 = \sum_{n=1}^{N} \frac{f_n \hbar^2 \omega_p^2}{\mu_{ST}^2 E_n^2} \tag{18}$$

Table 5 displays the minimum energies and speeds for water and the constituents of Betamax:

Name of Compound	Minimum Speed	Minimum Kinetic Energy (MeV)
Water	0.863	0.870
Alkylate 225	0.819	0.691
PXE	0.815	0.676

Table 5: Calculation of minimum speeds and kinetic energies for which the density correction applies

The stopping powers of the compounds are then determined using Equation 9, with Δ=10 keV. The stopping powers for the compounds that make up Betamax are shown in Figure 15.

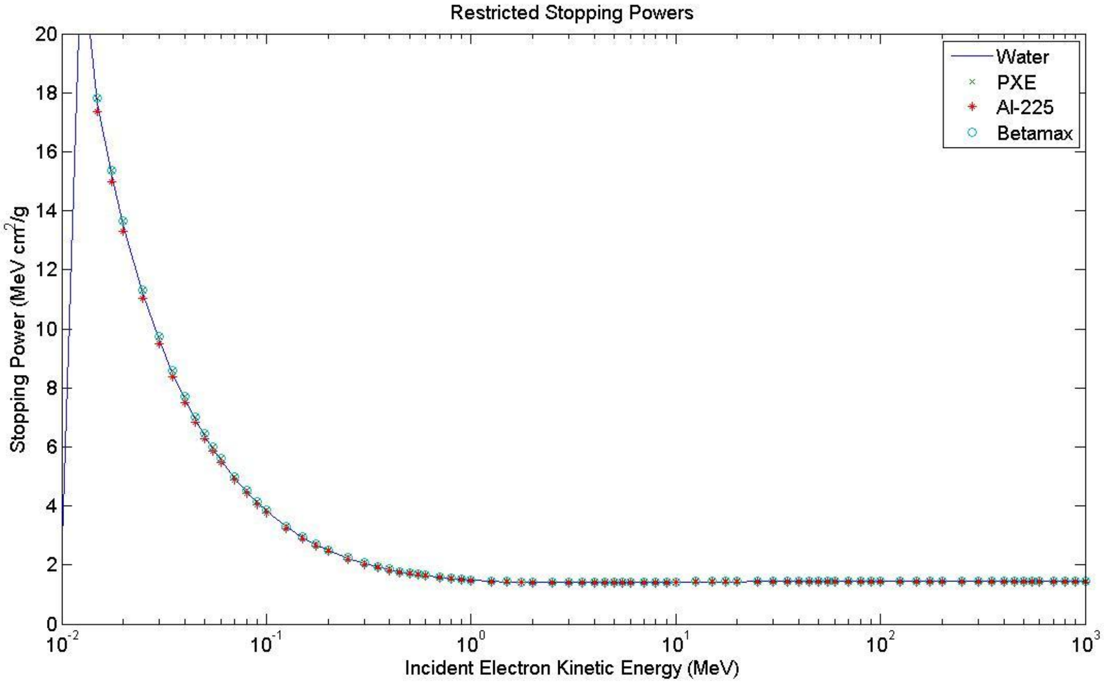

Figure 15: Restricted stopping powers for Betamax's constituents as well as water as calculated with the ICRU 37 protocol.

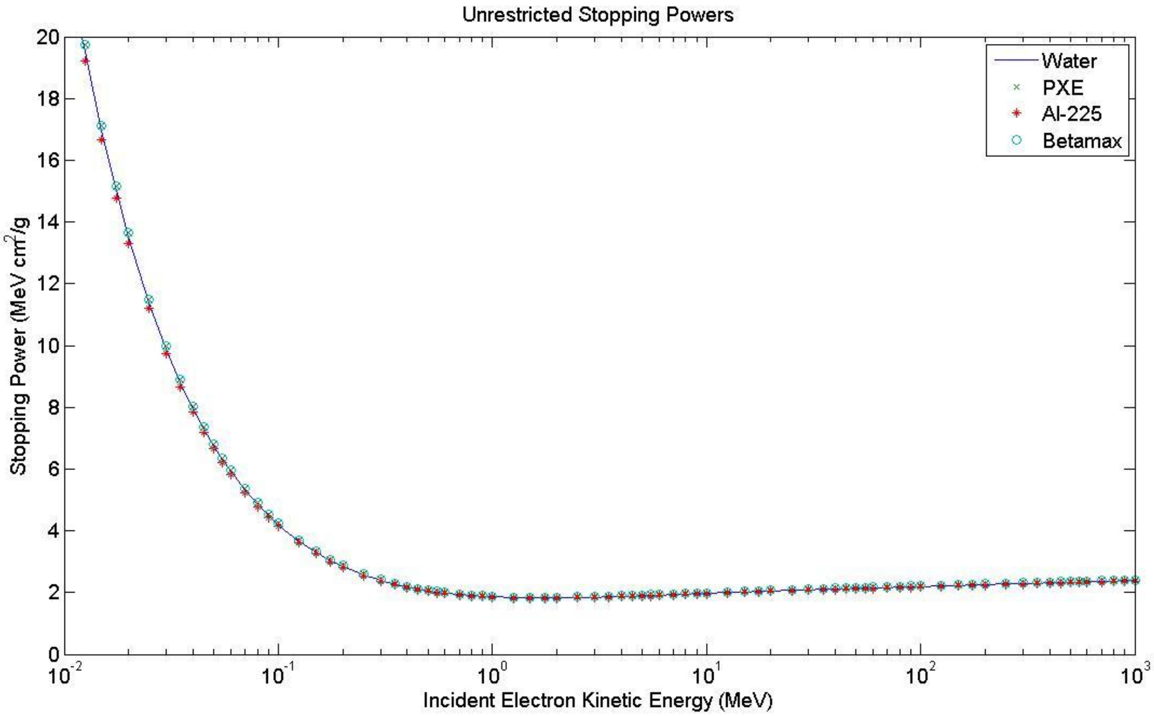

Figure 16: Unrestricted stopping powers for Betamax's constituents as well as water, as calculated with the ICRU 37 protocol

3.4 SPRRZnrc

SPRRZnrc is a user code that is distributed with the EGSnrcMP Monte Carlo package and it computes either the restricted or unrestricted stopping power ratios for arbitrary user defined materials. Interactions in the medium f interest are broken down into a number of different components, designated as α, β, γ and δ interactions. The α interactions are those in which the electron's energy is above Δ both before and after the interaction has taken place. The γ interactions occur when the particle begins with energy above Δ but during the course of the interaction its energy falls below Δ. The δ events involve electrons or photons that are terminated because they fall below either the AP or AE values for photons and electrons respectively. The AP and AE values are global minimum energy cutoffs for photon and electron transport set in EGSnrc and particles that have energies below these energy cutoffs are terminated and their energy is deposited locally. Lastly, the β events are those in which the photons or electrons were below AE or AP when first created.

The α events are handled by summing the energy deposited in the first medium and multiplying by the ratio of restricted stopping powers at the middle of the energy step to get the energy that would be deposited in the second medium.

There has been much deliberation as to how to treat the β events and no consensus has been reached. The β events are scored only in the evaluation of total dose and SPRRZnrc outputs the restricted stopping power ratio both with the β events included and with β events ignored and there is no significant difference between the two values.

In δ events the energy deposited in the first medium is scored and the same energy deposited multiplied by the ratio of unrestricted stopping powers evaluated at energy level Δ.

γ events are broken up into two stages, one with energy above Δ and the other with energy below Δ.

The total restricted stopping power ratio is then output as a combination of the events listed above. Note that with proper changes to the input files, unrestricted stopping power can be computed instead of the restricted stopping power ratios.

3.5 Verification of EGS Code

Whenever new Monte Carlo simulations are performed, one has to benchmark the code with previous results to ensure that there are no egregious errors in coding. The same code used for Betamax was initially run with water and air as the two media. This was done because the stopping powers for air and water have been determined in previous investigations. Thus the results of this code can be compared with previous values for a general verification of the code.

Figure 17 shows results of the comparison. The right subplot shows the restricted and unrestricted stopping powers as calculated by the ICRU formalism, as well as the stopping powers quoted by the NIST website. The very good agreement between the NIST data and the ICRU calculated data indicates that the ICRU formalism is still valid, and can be applied to our Betamax model. The left subplot has the stopping power ratio (water/air) given by NIST, the restricted and unrestricted stopping powers as calculated by the ICRU formalism as well as the restricted and unrestricted stopping power ratios as calculated by EGS. Restricted stopping powers and unrestricted stopping powers differ in that restricted stopping powers only consider collisions with energy transfers smaller than a chosen cut-off energy, Δ. Again, very good agreement is seen between all three sources, which indicates that the stopping power ratios given by EGS for these input files is valid.

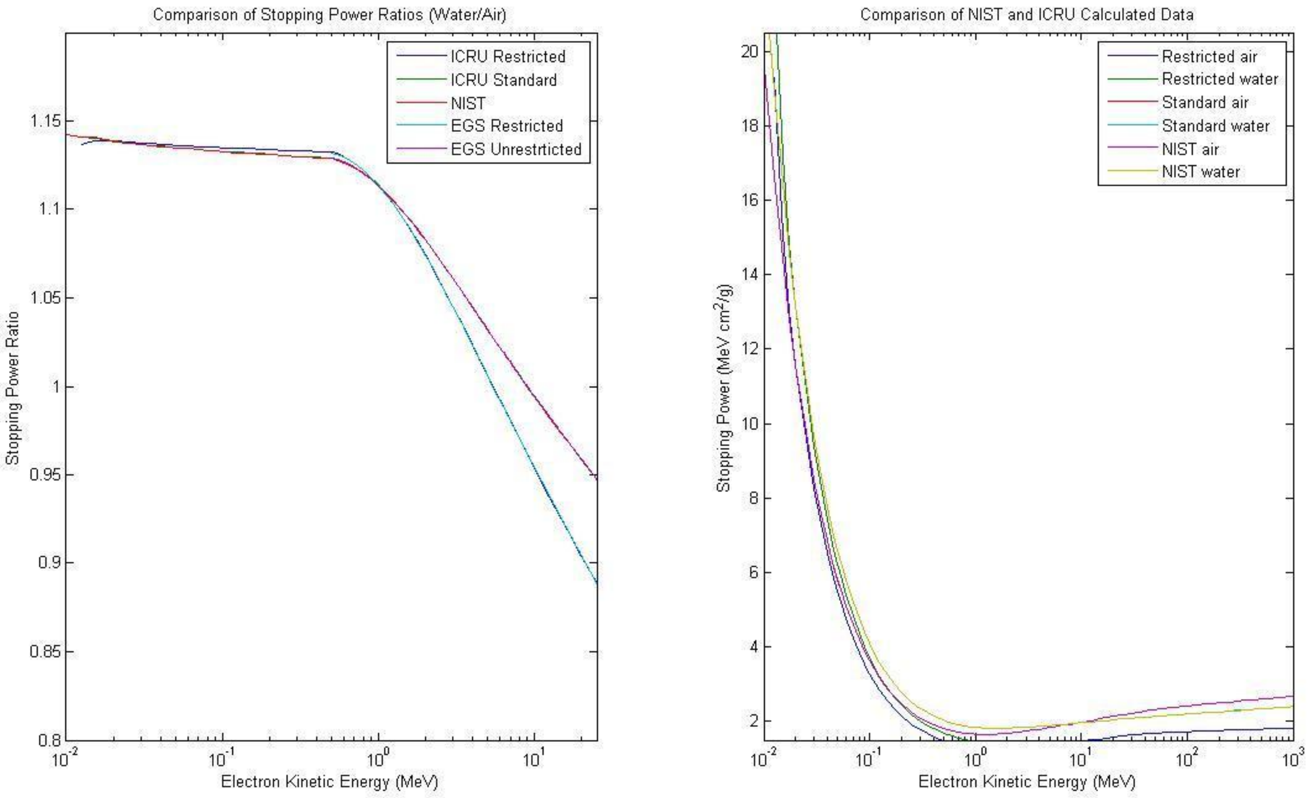

Figure 17: Left: verification of Betamax code by using air and water as media and comparing with NIST data and ICRU 37 calculation of stopping power. Right: verification of ICRU 37 calculation by comparing with NIST data.

3.6 Implementation of EGS code

The same input file as used in obtaining the water and air data as displayed in the Figure 17 was then used to calculate the SPR for water to the constituents of the Betamax. Figure 18 shows the unrestricted stopping power ratios for water to the Betamax constituents that have been compiled from ESTAR, EGS and our ICRU 37 calculations. The circles represent the EGS code data, the stars represent ESTAR data and the lines show our calculations from ICRU 37. Very good agreement can be observed from all three sources, except for the very low energies. This can be explained by variations in the mean excitation energies used in this work versus NIST.

The stopping power ratios are all close to unity over a large energy range, which means that the presence of a Betamax-based detector will not have a significant impact on the fluence of particles within a patient or phantom. This was one of the biggest advantages of using a scintillating material as a detector over a non-water equivalent ion chamber (as stated earlier) and based on our model, that this has been verified.

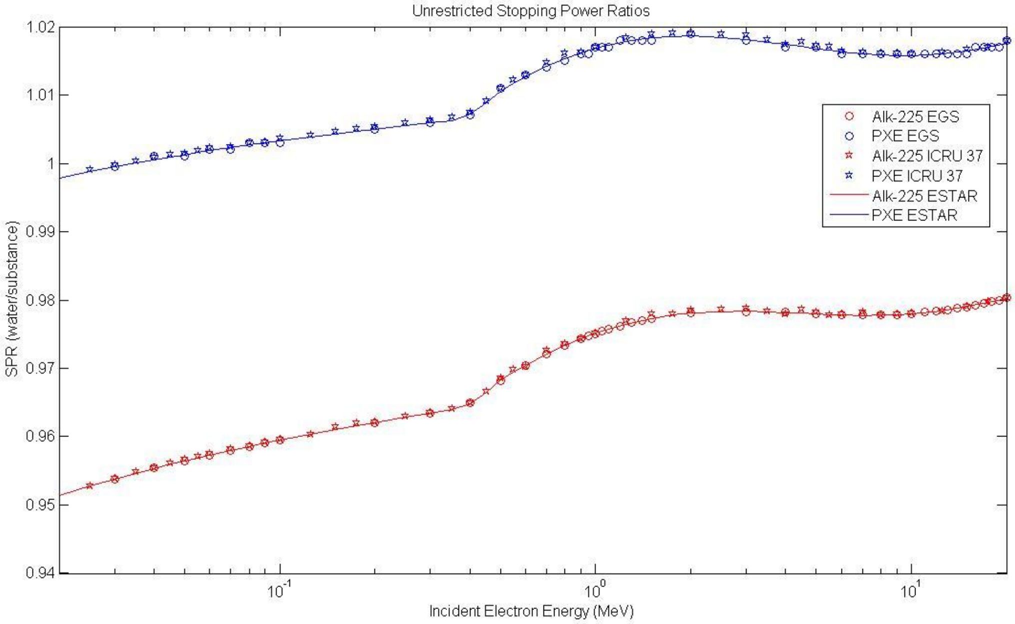

Figure 18: EGS, ICRU 37 and ESTAR stopping power ratios for water to Betamax's constituents

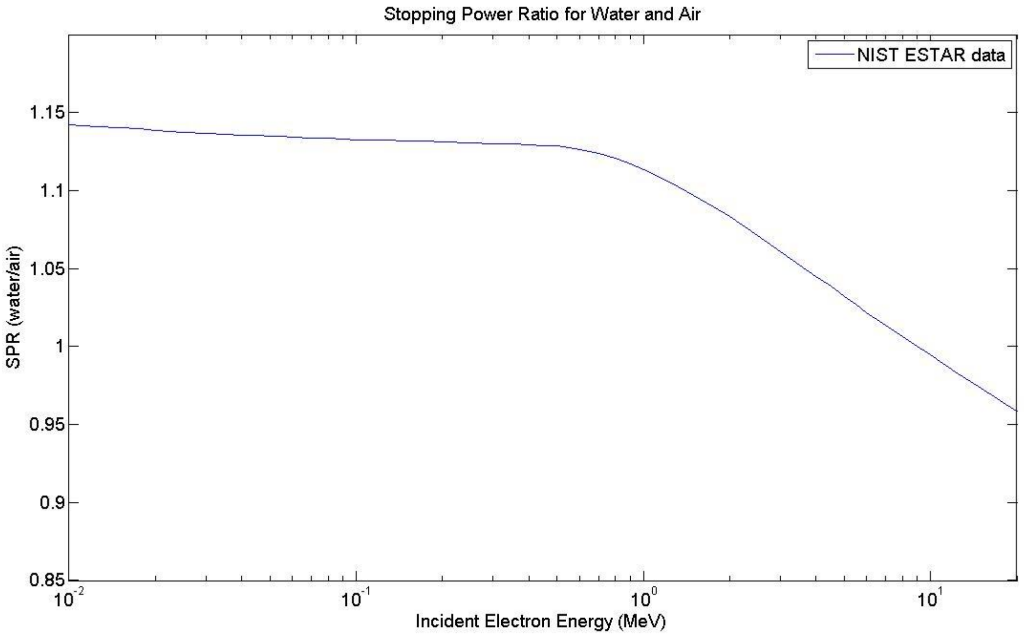

Figure 19: Stopping power ratio of water to air

3.7 Detector Hardware

3.7.1 Webcam/CCD

The premise underlying this project is to create an inexpensive and easy to use dosimeter that also yields good spatial resolution. Another requirement of the detector system was that it could be connected to any computer via a USB connection. This lead us to investigate the usage of webcams.

The general procedure when starting to integrate a webcam into the detection system was to remove all of the exterior casing until all that remained was the CCD, which was embedded onto a printed circuit board. The circuit board has a USB connection that was inserted into a laptop. The computer had been pre-loaded with Matlab R2009b, which included the Data Acquisition Toolbox. Originally, we had tried to acquire the data from an initial webcam (Xbox Live

Vision, Microsoft, Albuquerque, NM) with freeware obtained from the Matlab website, but this software was found to be insufficient for our needs.

The webcam that is used is the Philips SPC880NC webcam. This webcam is frequently used for amateur astronomy photographers due to its very low noise levels which are required for long astronomy exposures. The low noise level solved the most significant problem encountered with using simple webcams, while still keeping the cost low.

The SPC 880NC employs a Sony ICX098BQ CCD. The CCD is able to produce a maximum image resolution of 640x480 pixels, with each pixel being square with a side length of 5.6 μm.

3.7.2 Scintillation Container

The scintillation container was designed to match the Protea cylindrical ion chamber's external physical dimensions and location of sensitive volume. It was decided to match the Protea detector because of its relatively small volume for an ion chamber and a radiological water equivalent plastic (solid water, Gammex, WI) slab had already been created to house this ion chamber. Clinically, the Protea detector is used at the Cross Cancer Institute, where this work was carried out, in quality assurance of electron cutout factors as well as IMRT plan modulation factor verification.

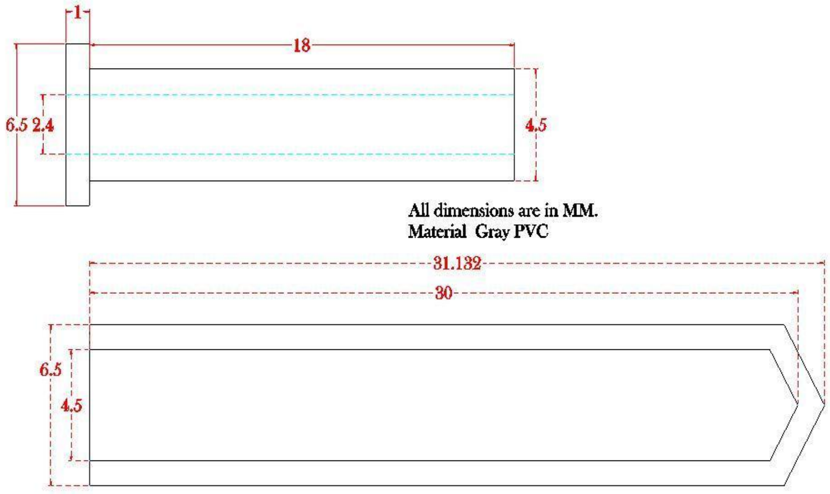

Figure 20: The schematic diagram of the scintillator container

Figure 20 shows the CAD drawing that was used to produce the scintillation container. The top structure (plug) was inserted into the lower structure and then glued in place. The central bore hole in the top structure is just big enough to allow one of the two fibers from the duplex cable to be inserted. The fiber that was not inserted was cut 19 mm shorter so that it would terminate just short of the end of the container.

The drill bit used created an 118° angle at the furthest extent of the container, and therefore the internal volume of scintillating fluid is approximately 0.198 cm^3.

The geometrical specifications of our ion chamber were obtained from a technical document from Protea Systems Corporation. The document gives an outer diameter of 6.5 mm, and inner diameter of 4 mm and an active length of 12 mm.

The scintillation container was designed to have an active length of 12 mm to match the active length of the active volume of the ion chamber. We were also able to produce thinner walls, which, along with the lack of a need for a central electrode, accounts for the larger active volume. The total length of the chamber is 30 mm, which is almost identical to the scintillation container, which is 31 mm.

The plug has two functions: the first is to act as a cap for the container to provide a seal and the second is to offset the location of the center of the scintillation fluid. If the centers of the two detectors were not at the same location, the particle fluences in the scintillation container and ion chamber would not be the same and the phantom would have to be shifted accordingly between measurements.

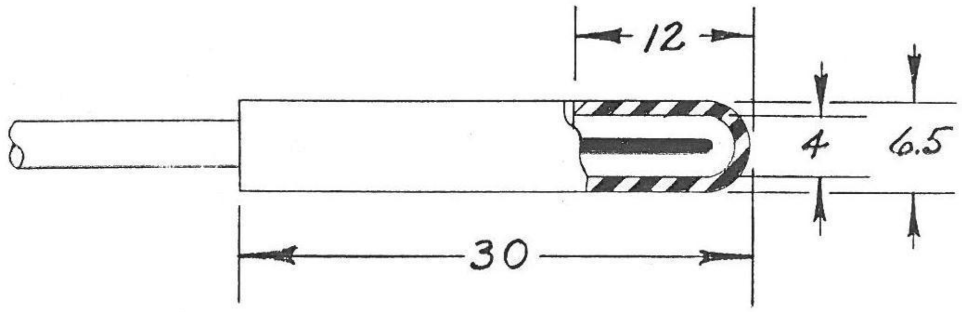

Figure 21: Diagram of Protea Detector taken from technical document. Note that all dimensions are reported in millimeters

After the optical fiber was inserted into the plug, the two were fastened with a clear silicon. This has to be done very carefully because if any of the liquid scintillator is present on the adhering surfaces the silicon will not solidify and therefore a good hold will not be established.

The choice of PVC as a container was made because the scintillation liquid did not appear to have any reactions with the PVC. The scintillation container that is currently being used is the result of several prototypes failing, one of which failed due to the scintillator disintegrating some of the plastic casing and subsequently becoming discolored.

3.7.3 Fiber Optic

The fiber optic cable was a duplex plastic core fiber produced by Industrial Fiber Optics Incorporated in Arizona. Technical documents on the supplier's website indicate a typical core diameter of 980 μm surrounded by 20 μm of cladding (Digi-Key, MN). Encapsulating the cladding is a black polyethylene jacket making the entire fiber which has a nominal diameter of 2.2 mm. As previously mentioned, the cable is duplex, meaning that two fibers are connected and run parallel throughout the length. The total length of the fiber is 1 m, meaning that the CCD detector would have to be in the room and therefore it would have to be shielded. The attenuation of the fiber is 0.14 dB/m, yielding a total attenuation of approximately 3.2% over the length of the fiber.

One of the advantages of using a liquid scintillator in the fashion that we've used it here is that coupling of the optical fiber to the scintillator is not necessary as it is immersed in the liquid. This can be a drawback of the use of plastic scintillators or scintillating fibers as good polishing techniques have to be employed to avoid losses (Lacroix, et al., 2008). The optical coupling of the fiber optic to the CCD face was accomplished by first cutting the end of the fiber optic with a scalpel and then physically abutting the fiber optic to the CCD cover plate.

A plastic holder was designed and implemented that would ensure good physical contact between CCD and fiber optic, as well as isolating the CCD from ambient light.

Under the assumption that scintillation photons are isotropically emitted the probability of photon capture by the optical fiber was calculated. The calculation was done assuming only a two-dimensional chamber but due to the cylindrical symmetry of the chamber, the three-dimensional distribution can be extrapolated.

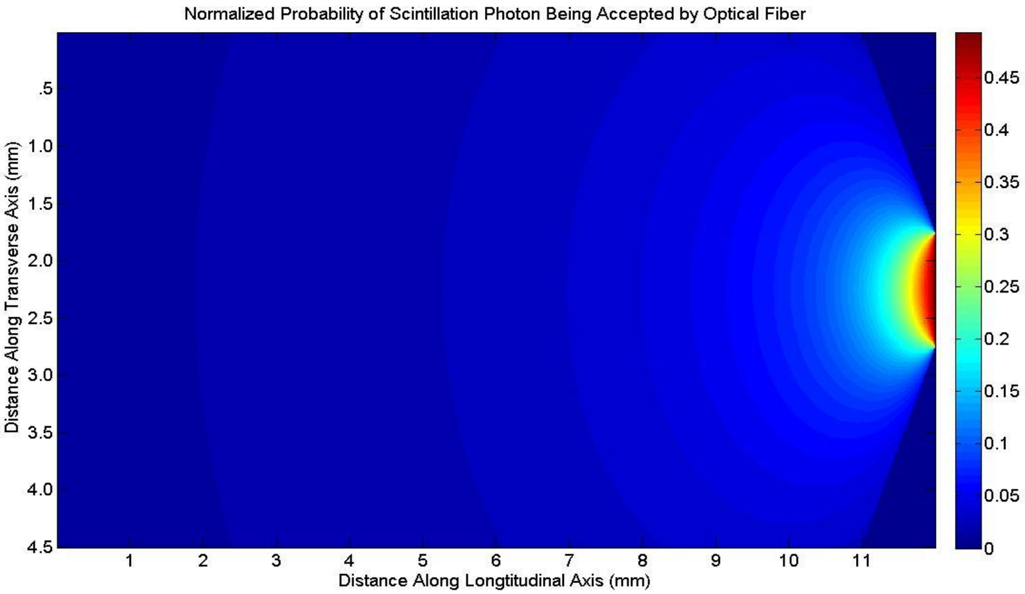

Figure 22: Probability of a scintillation photon being captured by optical fiber in 2D plane

Figure 22 shows that the probability of an emitted scintillation photon being accepted into the fiber optic drops sharply as the distance between the point of emission and edge of the fiber optic is increased. This is due to the fact that the angle subtended by the fiber diminishes with increased distance between fiber and emission point. The data shown in Figure 22 would also suggest that the size of the container is much larger than what is needed. Note that this has assumed that there is no reflection of photons at the surfaces of the container and that there is no self absorption in the scintillator.

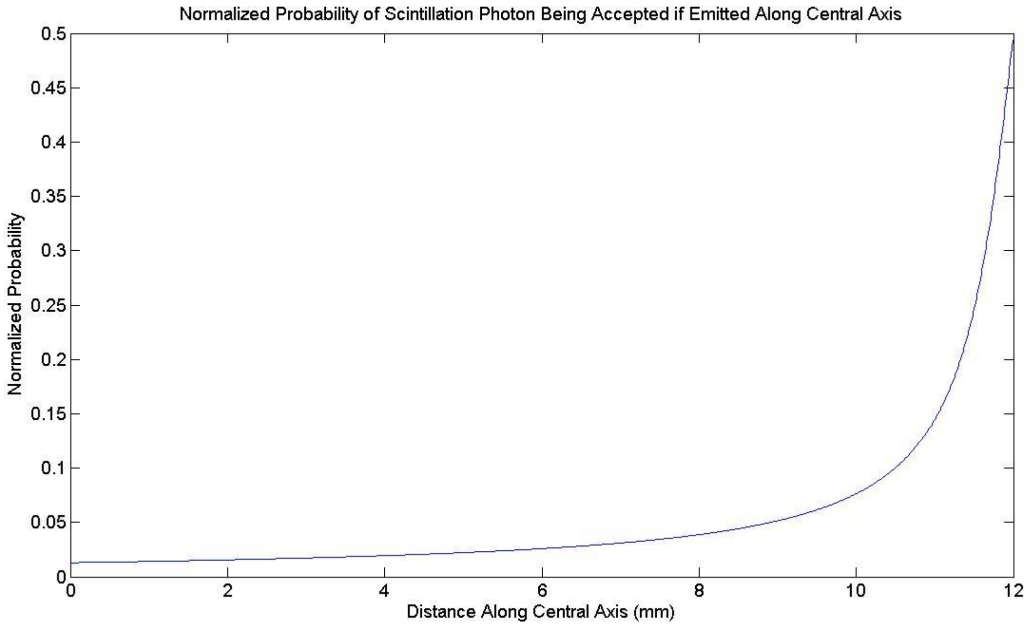

Figure 23: Normalized probability of a scintillation photon being captured by optical fiber if emitted along central axis of detector

The fiber optic has a large plastic core roughly 1 mm in diameter. There are other fiber optic wave guides with glass cores that have much smaller cores (56 μm diameter or smaller). One of the benefits of this is that one could have many more signal inputs onto a CCD, meaning that a given CCD could measure the signal from several detectors at once. Furthermore, having the smaller core would produce less Cerenkov radiation due to decreased material. A very long (~20m) glass-core Corning Infinicor (Corning Incorporated, Corning NY) cable was purchased to compare our cable with a smaller-core fiber. When preliminary measurements were taken with the fiber, very little signal was observed to pass through the fiber. I believe this was due to the fact that we don't have the required specialized polishing equipment that would be needed to get good transfer acceptance at the ends of the fiber and if this equipment was available the glass-core cable could still be utilized. . The refractive indices the cores of our fiber optic and the glass fiber optic are 1.492 and 1.496 respectively.

3.7.4 Shielding

Because CCD's are damaged when they irradiated with ionizing radiation, we needed to come up a design for a small shielding container to prevent damage. The goal was to have enough material to reduce an incoming 6 megavolt (MV) photon beam by at least 90%. The decision was made to go with lead shielding, since it could be easily constructed in the medical physics department's machine shop. To calculate how much lead would be required for we use (Johns & Cunningham, 1983):

$$N = N_0 e^{-\mu x} \tag{19}$$

Given that the mass interaction coefficient for lead at 6 MeV is 0.00429m^2/kg and the density is 11360kg/m^3 (Johns & Cunningham, 1983), we obtain:

$$x = \frac{\ln(10)}{\mu} = \frac{2.30}{0.487cm^{-1}} = 4.72\ cm \tag{20}$$

We would therefore require at least 4.72 cm of shielding to reduce a beam of entirely 6 MeV photons to 10% of its beginning fluence. It was decided to round to 5 cm of material for simplicity.

The interior dimensions of the lead box were $95 \cdot 70 \cdot 105$ cm^3 which is greater than required for our final detector. This is because an older model of our detector had a black plastic box built around it that required those dimensions.

A program called Google Sketchup 8 was used to create diagrams of the shielding and the diagrams are shown in Figures 24, 25 and 26.

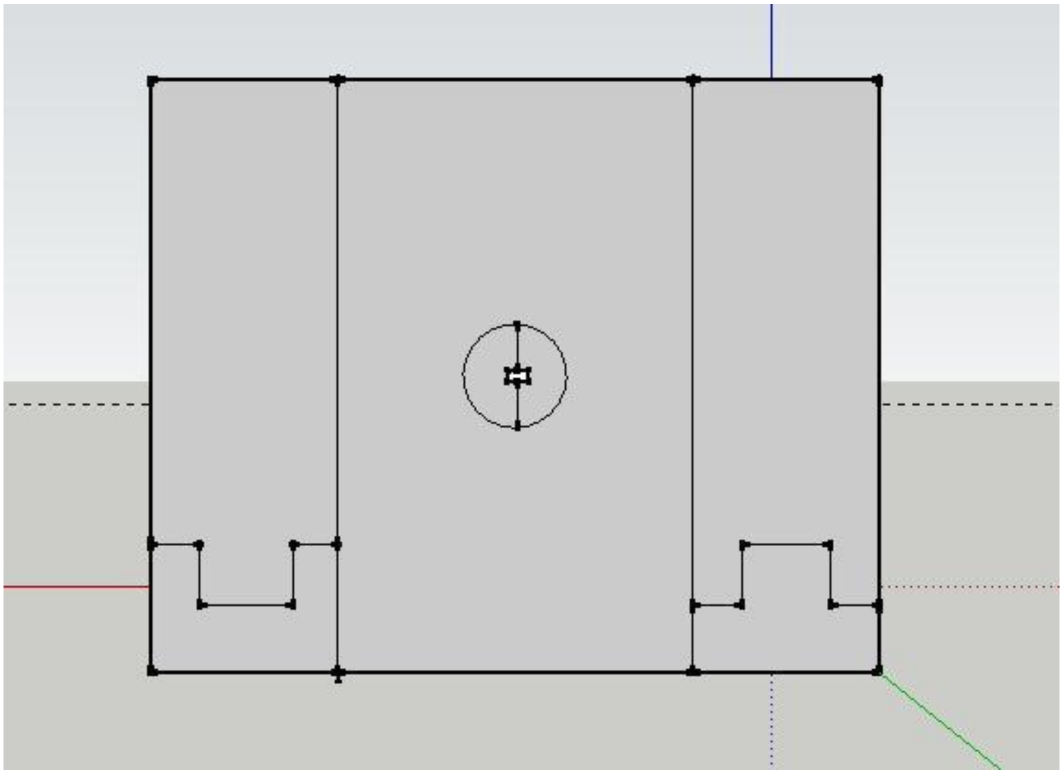

Figure 24: Diagram of front face of shielding

Figure 24 shows a view of the front face of the shielding. The circular center object is removable and allows the user to easily insert the fiber optic cable through the opening. The object is composed of two semi-circular halves that encapsulate the fiber for the full length of the shielding (5 cm). Note that the vertical seams are the only place in the shielding where there is a straight line shielding join: all of the other seams between the lead pieces are interlocking.

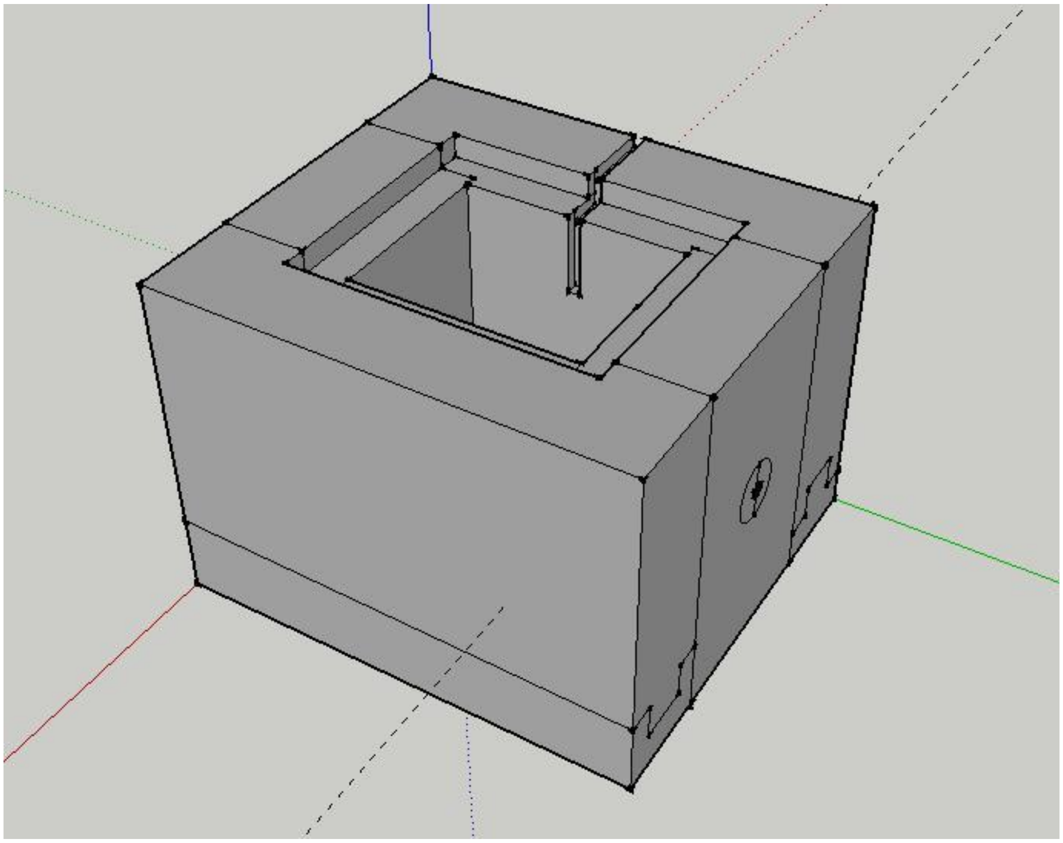

Figure 25: Diagram of shielding viewed from above

Figure 25 shows a three dimensional view of the shielding with the lid removed. The only detail that is not included in this image are two screws that attach each of the side vertical panels to the front and back vertical panels. There is a groove cut into the distal vertical side panel that allows for the CCD's USB cable to exit the shielding. The groove was intentionally made to be not straight to increase the quality of shielding.

Figure 26 shows the lid. This simply fits into the top of the shielding to give shielding from every direction.

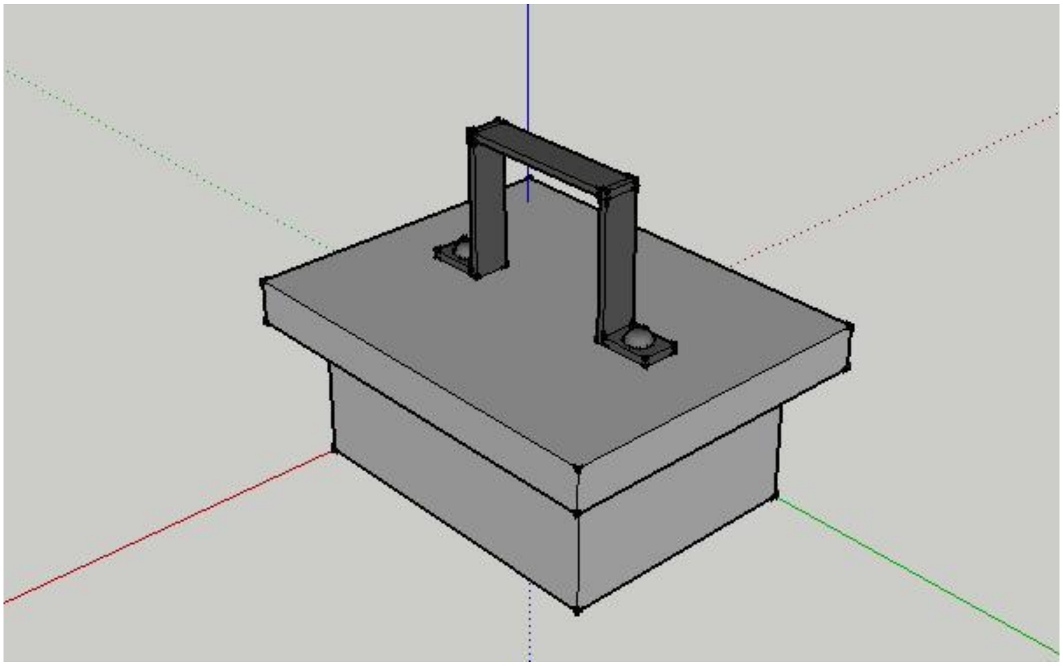

Figure 26: Diagram of shielding lid

3.7.5 USB Extension Cables and Computer

Because our fiber optic cable was only one meter long and the computer could not be in the linac treatment vault during operation, we purchased three five meter USB extension cables, each five meters in length. The cables have a USB 2.0 interface and are able to transmit enough power to allow the camera to operate without an additional power source.

The computer that is used for all of the acquisitions is a Dell XPS 1340 laptop. It should be noted that all that is required is that the RAM of the computer may have to be upgraded for long acquisitions, otherwise most any computer will do, given the proper software (e.g., Matlab). During preliminary runs that were attempting to measure the heating of the CCD, some of the acquisitions exceeded the 4 GB of RAM that was installed on the laptop. This has not been found this to be a problem since initial runs, however, since actual acquisitions of interest seldom last longer than a few minutes.

3.8 Solid Water Slab Chamber Housing

A radiologically water-equivalent slab of plastic (Solid Water, Gammex, WI) had previously been constructed to house the Protea detector. The slab is 1 cm deep, 25 cm long and 25 cm thick. A 5 mm by 7 mm channel was cut along the middle to allow room for Protea's cabling. In the middle of center of the slab was a circular cutout measuring approximately 57 mm in diameter. The purpose of the cutout is to allow the user to insert the ion chamber into the slab; the user first inserts the chamber into the cut-out and then the cutout is lowered into the slab. The slab was meant to be used in conjunction with a set of solid water slabs of varying thickness that could be used together to build a phantom. The scintillation detector housing was designed to match the geometry of the Protea ion chamber so that this solid water slab housing could be employed for our measurements.

Figure 27: Photograph of solid water slab with insert to house ion chamber.

3.9 Acquisition Software

The software used to acquire the image is a freeware package named SharpCap that is available online. Data acquisition with previous webcams had always been done in Matlab, but the user is unable to specify the auto exposure setting in Matlab, so a new program had to be used. The decision to go with SharpCap instead of other similar programs was made for several reasons:

- The program was free and no licensing requirements had to be met.

- The program would output a unique filename with each video acquisition so that sequential acquisitions could be obtained without the need for immediate cataloguing.
- The program also output a text document with each acquisition that would name all of the imaging parameters used. This is a good feature when reviewing older acquisitions.
- Any imaging parameters could be easily changed on-the-fly, whereas in Matlab they couldn't be changed during an acquisition. Additionally, the program is much more user friendly than the Matlab package.
- The user can define various imaging parameter sets, which can be used to easily select a set of parameters. This would allow the user to define a parameter set that is optimized for each type of measurement required.

After each acquisition, the data is saved in Audio Video Interleave (avi) format for future processing in Matlab.

3.10 Matlab Video Processing

There are three programs that have been written to process the video data once it has been recorded. The three programs have different functions that are all necessary for accurate interpretation of the data.

3.10.1 Setting Signal and Cerenkov ROIs and Compensating for Coupling Efficiency Differences

There are two initial acquisitions that are required to be taken before the user can start to take measurements on a given day. These two acquisitions will be described below.

The first program that is employed allows the user to select where the Cerenkov region of interest is. The region of interest is selected to be around where the Cerenkov fiber contacts the CCD face. To accomplish this, the user takes a short acquisition with very high gain and exposure settings. During this acquisition, there is no irradiation and so only dark noise is detected. This is done because the blacking out of the Cerenkov fiber is not perfect and with high gain, high exposure setting, with all of the lights on in the treatment vault and with the detector not inserted into the slab, the user can see where the light that is transmitted through the blacked out end and onto the CCD.

When the Matlab program is run, one of the frames from the acquisition is displayed and the user is asked to click where he/she would like the center of the Cerenkov ROI to be. The region of interest is then selected as a square box surrounding the central pixel with full length of 30 pixels in both the vertical and horizontal direction. This ROI data is saved for use in subsequent program use.

The user then performs a series of identical sequential irradiations where only the two fibers are irradiated and the scintillating volume is not in the beam. The signal detected by the CCD is essentially only Cerenkov radiation that is produced in each of the fibers. This performs two functions:

1. The location that the scintillation fiber contacts the CCD face is now visible to the user. The Matlab program now asks the user to select the scintillation region of interest exactly as was done for the Cerenkov ROI.

2. The ratio of the signal measured between the two fibers is calculated. This is done to correct for the fact that there can be a discrepancy between the coupling efficiency between each fiber and the CCD.

To determine the ratio of the signals of the two fibers, a few steps are employed. First, the user is queried to select an offset that will eliminate the dark current signal. The user then looks at the measured signal and tells the program where the time cutoff exists between sequential irradiations. The program then sums the total signal value arising from each ROI and the fraction of signal from the 'signal' ROI to the signal from the Cerenkov ROI is computed. This will be used in later processing of data.

3.10.2 Processing Acquisition Data

After the two ROIs have been set, one is ready to start taking data acquisitions. When the user begins the program, they select an .avi file from an acquisition and the video data is loaded into Matlab. The resultant data is yielded in an M x N x F array, where M is the total number of horizontal pixels in the CCD, N is the total number of vertical pixels in the CCD and F is the total number of frames acquired. This data is then broken up as dictated by the two user-selected ROIs, yielding two separate 30x30xF matrices. The program then sums over all of the pixel values for each individual frame to create a 'sum of signal values' array with F frames for both the Cerenkov and signal ROIs. This 'sum of signal values' will henceforth be referred to as SPV.

The program then displays the SPV array as a function of time and asks the user if it appears to the user as if one DC offset is sufficient. A DC offset has to be employed because even when there is no irradiation, the pixels do not necessarily record a zero value. This occurs because of capture of thermal electrons. Because the capture of these electrons is temperature dependent and the temperature increases as the CCD is operating, care has to be taken when using a DC offset. If one DC offset for the entire acquisition is not sufficient, the user will see that the background signal appears to increase in time and the user is allowed to select 'No' as a response to the program. If this is the case, the DC offset is applied to each sequential irradiation independently. The issue of CCD heating was a significant issue with the first CCDs that were used, which is why this functionality as employed, but if the user turns on the camera and lets it heat up prior to taking acquisitions this is no longer a problem with the current CCD as it reaches steady state. The DC offset is applied to both the signal ROI and Cerenkov ROI SPVs.

To apply the DC offset, the user is asked to specify a SPV quantity that distinguishes between when the beam is obviously off and when it is on by clicking on a point of the plot. A sub-program then sums the SPVs from each frame where the SPV falls below the cutoff and divides this value by the total number of frames where this condition is met. This gives an average value of the background signal and this value is subsequently subtracted from every SPV.

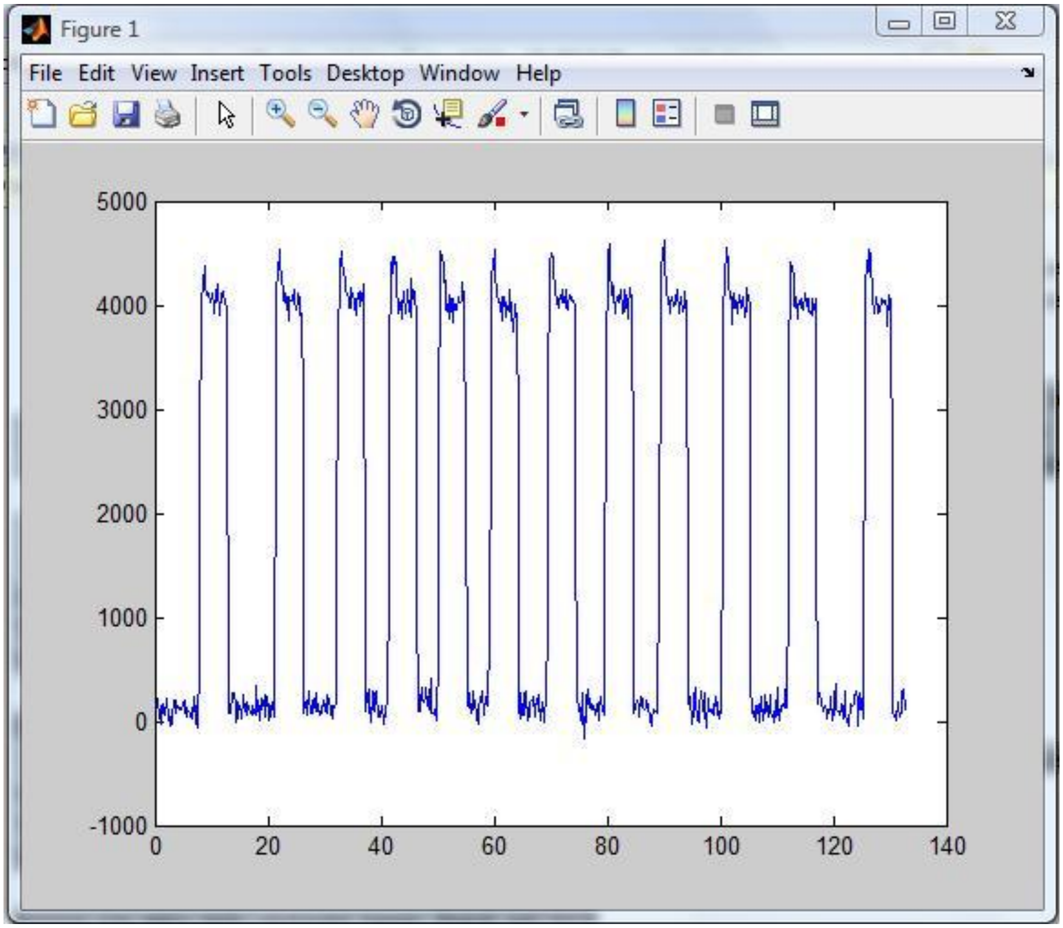

Figure 28: Example of interface allowing user to select DC offset level and beam timing

Figure 28 shows what a user would see for a sample acquisition where 13 sequential irradiations were measured. Popup boxes guide the user through analysis and the user can click on the plot to send information to Matlab.

Because there is no functionality written into the Matlab script to distinguish between separate irradiation periods, the program again displays the SPV array as a function of time and the user selects appropriate time cutoffs for each sequential irradiation. This allows the program to analyze several sequential irradiations with a single acquisition which reduces the number of files required and can speed up processing.

At this point, the DC offset is applied and then the scaling of the SPVs from the two ROIs acquisition is implemented. As mentioned previously, the scaling is used to take into account the fact that the coupling efficiency between the two fibers will not be the same. It is important to apply the scaling after the DC offset has been applied, as the scaling factor was originally determined after the DC offset correction had been applied.

Once the user has distinguished between sequential irradiations, the program sums up the SPVs for each irradiation. These quantities represents the total signal measured for each irradiation. The program finally outputs this data to the user for analysis and plots the measured SVP as a function of frame number for both ROIs. An example of the sample output is displayed below.

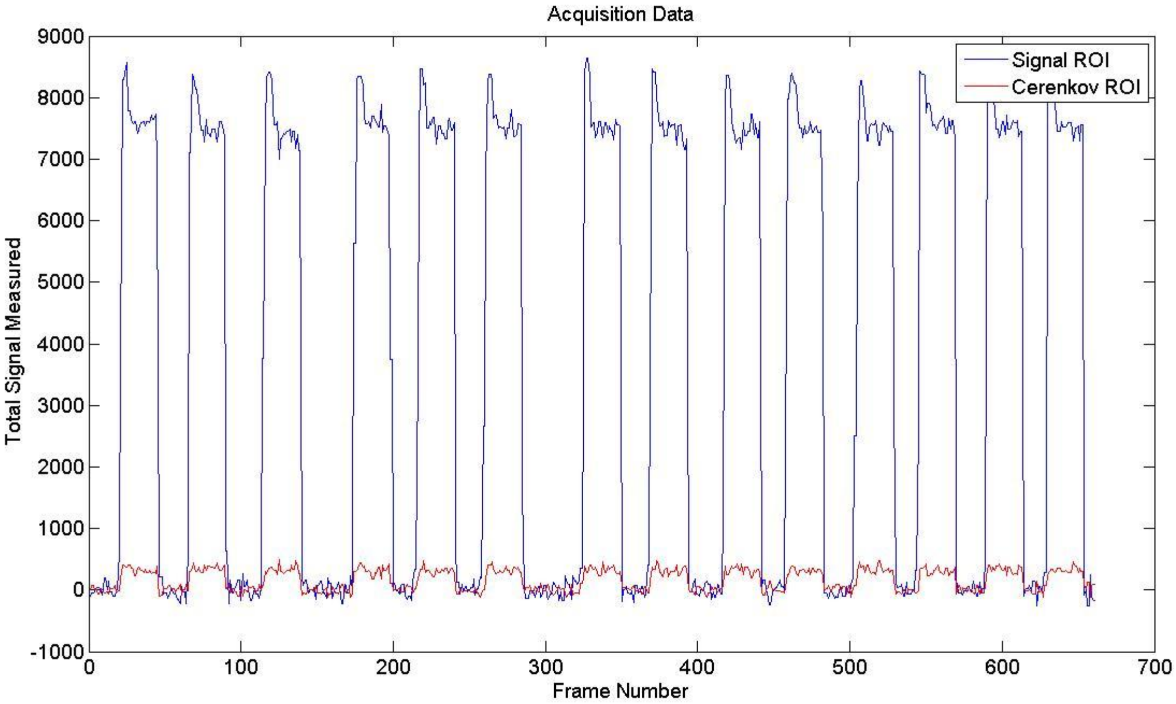

Figure 29: Example output from Matlab program

3.11 Outline of Procedures for Dosimetric Measurements

3.11.1 Verification of Independence of Dose Rate

A series of measurements were taken on a Varian Trilogy iX linac to verify that the scintillator detector was not dose rate dependent. The detector was inserted into in a solid water slab that was placed on the linac's couch and there was 11 cm of solid water backscatter placed below the slab phantom, for a total of 11.5 cm of backscattering material. Two centimeters of solid water was placed on top of the slab phantom such that there was a total of 2.5 cm of buildup material.

The height of the couch was set initially so that the center of the detector was at 100 cm SAD and then the couch height was varied from outside of the room. For each couch height an acquisition was obtained with twelve measurements of 50 monitor unit (MU) irradiations with a dose rate of 600 MU/min at the couch height of interest as well as the couch height corresponding to 100 cm SAD. The beam energy was 6 MV. The 100 cm SAD measurements were repeated for each acquisition in order to monitor any drift in baseline measurements that might occur.

There were a total of eight couch heights that were measured, corresponding to 90, 95, 100, 105, 110, 115, 120, 125 and 130 cm SAD, meaning that a total of 96 measurements at 100 cm SAD were taken over 65 minutes of acquisition.

After the scintillator detector measurements were taken, the Protea ion chamber was inserted into the solid water slab phantom and the measurements were repeated to ensure that the trend observed with the scintillation detector is what should be expected.

3.11.2 Measurement of Physical Wedge Factors

The physical wedge factors were measured on a Varian Trilogy linac. To perform these measurements, the scintillator detector was placed in a solid water slab phantom that provided 11.5 cm of total backscattering material and a total of 2.5 cm of total buildup. Note that this is the same setup as for the inverse square measurements. The detector was placed at 100 cm SAD and 12 measurements of 50 MU, 600 MU/min were taken with for a 6 MV open field. The 15°, 30°, 45° and 60° wedges were then inserted into the interface mount in both the 'in' and 'out' directions along the Y axis and 12 measurements were taken for each wedge angle and orientation.

Following that, the scintillator chamber was removed and the Protea ion chamber was inserted into the slab and the measurements were repeated with two measurements of each wedge angle and orientation.

3.11.3 Measurement of Enhanced Dynamic Wedge Factors

EDW factor measurements were carried out using both the Protea ion chamber and the scintillation detector. The measurements were taken at 100 cm SAD with 11.5 cm of backscatter and 2.5 cm of solid water buildup. The beam energy was 6 MV, the dose rate was 600 MU/min and 50 MU were delivered for the open beam, while 100 MU was delivered for the wedged beams. In the standard protocol for measuring EDW factors, the open fields are measured with the same number of monitor units as the wedged field. The wedged field treatment was delivered with

100 MU's because that is how the quality assurance of EDW factors is done locally and we wanted to ensure consistency with the tabulated data for the linac.

3.11.4 Measurement of Relative Dose Factor

The relative dose factor measurements were performed using both the scintillation detector and the Protea ion chamber. The measurements were taken at 100 cm SAD with 11.5 cm of backscatter. Note that we used 0.5 cm of solid water buildup, instead of the 2.5 cm that has been used in the other measurements. Using 0.5 cm buildup was a mistake, because 0.5 cm of water does not provide transient charged particle equilibrium. Because the measurement was performed differently than how it should be performed, we will not be able to compare our results with tabulated data for the treatment unit. All measurements were taken with 6 MV beam energy at 600 MU/minute with a total irradiation of 50 MUs. Measurements were taken for square field sizes ranging from 10x10 cm^2 to 20x20 cm^2 in integer increments. Each measurement was performed twelve times with the scintillation chamber. Generally for relative dose factors the maximum field size is larger than 20x0 cm^2, but due to the size of the phantom, larger field sizes would extend beyond the extents of the phantom and the amount of scatter would be reduced.

3.11.5 Measurement of Tissue Maximum Ratio

The tissue maximum ratio (TMR), measurements were taken using the Varian Trilogy linac using 600 mu/min, with a 6 MV beam at 100 cm SAD. For this set of measurements, each repeated irradiation used a total of 100 MUs instead of the 50 MUs that have been used in other measurements. This was because with the large amount of buildup used the signal dropped fairly significantly, so larger MUs allowed us to obtain better statistics. A total of 11.5 cm of backscatter was placed on the couch and a varying thickness of solid water were placed on top of the slab to establish the TMR setup.

3.11.6 Measurement of IMRT Modulation Factor

The IMRT modulation factor is defined as the quotient of the signal measured in the treatment field to the signal measured in an open field.

The IMRT modulation factor measurements were taken using a Varian 23 EX linear accelerator. A typical patient 7-field low risk prostate IMRT plan was used to test the scintillation detector's ability to measure modulation factors. All measurements were taken at 100 cm SAD with 0° collimator rotation and 0° gantry angle. 10 cm of solid water was placed on the couch, yielding a total of 10.5 cm of backscatter material. 4.5 cm of solid water was placed on top of the slab to yield a total of 5 cm buildup. Measurements were taken in turn with both the scintillation detector and then with the Protea ion chamber.

Chapter 4: Results

4.1 Verification of Independence of Dose Rate

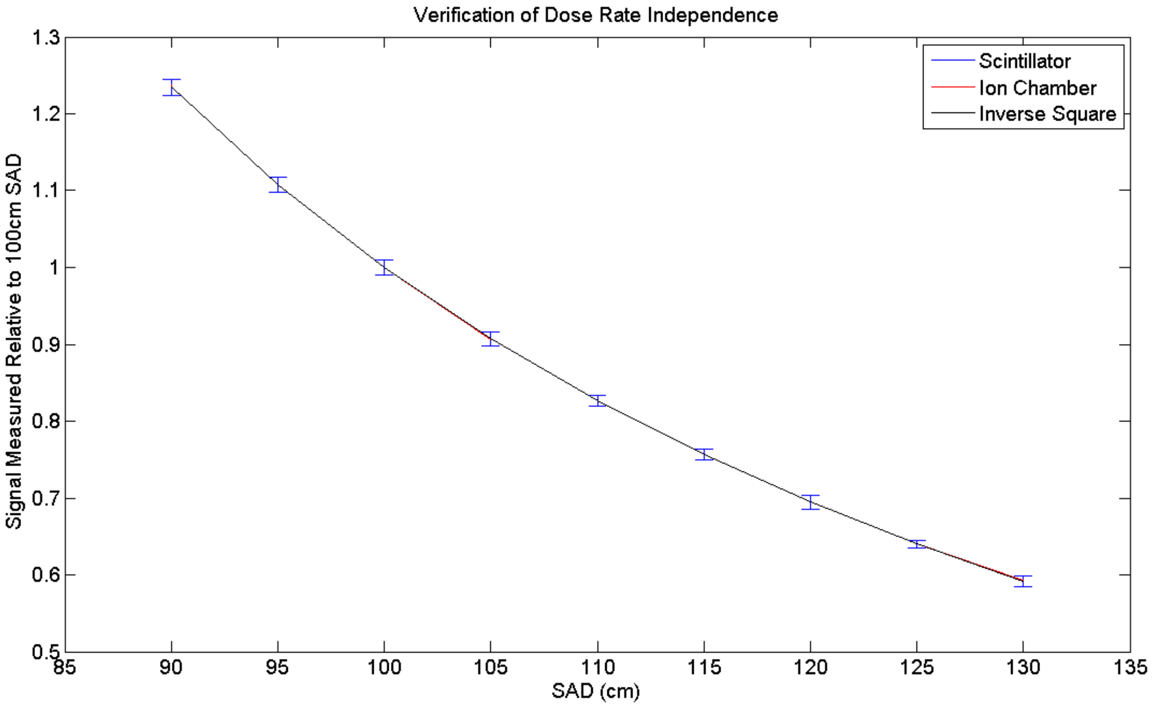

Figure 30: Verification of Dose Rate Independence

The results of the inverse square measurement are displayed in Figure 30. The ion chamber results and inverse square prediction agree so closely that the two lines are nearly indistinguishable in the plot. What is clearly visible in the figure is that the inverse square relationship is observed to the same extent as it is followed by an ion chamber. What this really means is that the signal measured by the scintillation detector is independent of dose rate, since the signal measured drops off in accordance with the increase in solid angle subtended by the beam (i.e. due to inverse square effect.)

SSD (cm)	Normalized Signal	Uncertainty in Normalized Signal
90	1.23	0.01
95	1.11	0.01
100	1.00	0.01
105	0.907	0.009
110	0.826	0.007
115	0.756	0.007
120	0.694	0.009
125	0.640	0.005
130	0.592	0.007

Table 6: Measurements of normalized measured signal as distance from source to detector is varied

The uncertainty in the normalized measured signal is displayed in Table 6. The uncertainty was determined by taking the standard deviation of the signal and using the method described in Appendix A to propagate the uncertainty.

Note that even if the detectors were truly dose rate independent, we should expect some disagreement between inverse square prediction and experimental results. Discrepancies can arise because the target focal spot has a finite size and scattered radiation is not reduced at the same rate. The formulation presented previously assumes that all radiation is being produced from a point source and since this is not the case we can expect the drop signal drop off to be less than what would be predicted for a point source.

4.2 Measurement of Physical Wedge Factors

Figure 31 displays the results of the wedge factor measurements, along with the values that have been previously determined for the machine in question. The values are also summarized in Table 7. There is no uncertainty displayed for Protea measurements because for the Protea chamber only two measurements for each data point were taken. The maximum fractional discrepancy between any two Protea signal measurements was 0.23 %. When wedge factors are measured monthly for machine quality assurance, the measurement is accepted as long as it agrees with the wedge factor determined during annual quality assurance to within 2 percent. All of the normalized scintillation signal measurements agree with this standard wedge factor within the uncertainty of measurements and the two percent acceptance window.

Field Type	Normalized Protea Signal	Previously Measured Wedge Factor	Normalized Scintillation Signal	Uncertainty in Normalized Scintillation Signal
Open	1.00	1.00	1.00	0.01
15° in	0.701	0.710	0.71	0.01
15° out	0.702	0.710	0.71	0.01
30° in	0.542	0.542	0.55	0.01
30° out	0.542	0.542	0.55	0.01
45° in	0.482	0.485	0.494	0.007
45° out	0.484	0.485	0.500	0.007
60° in	0.395	0.401	0.409	0.005
60° out	0.398	0.401	0.411	0.006

Table 7: Protea and scintillator signal measurement and standard machine data for wedge factors

4.3 Measurement of Enhanced Dynamic Wedge Factors

Figure 32 displays the results of the measurements that were taken. To obtain each scintillator data point, the measurement of both the Y1 in and Y2 out orientations were taken twelve times and then averaged to get a wedge factor. As can be seen in the plot, the scintillator measurements and ion chamber measurements all agree to within error.

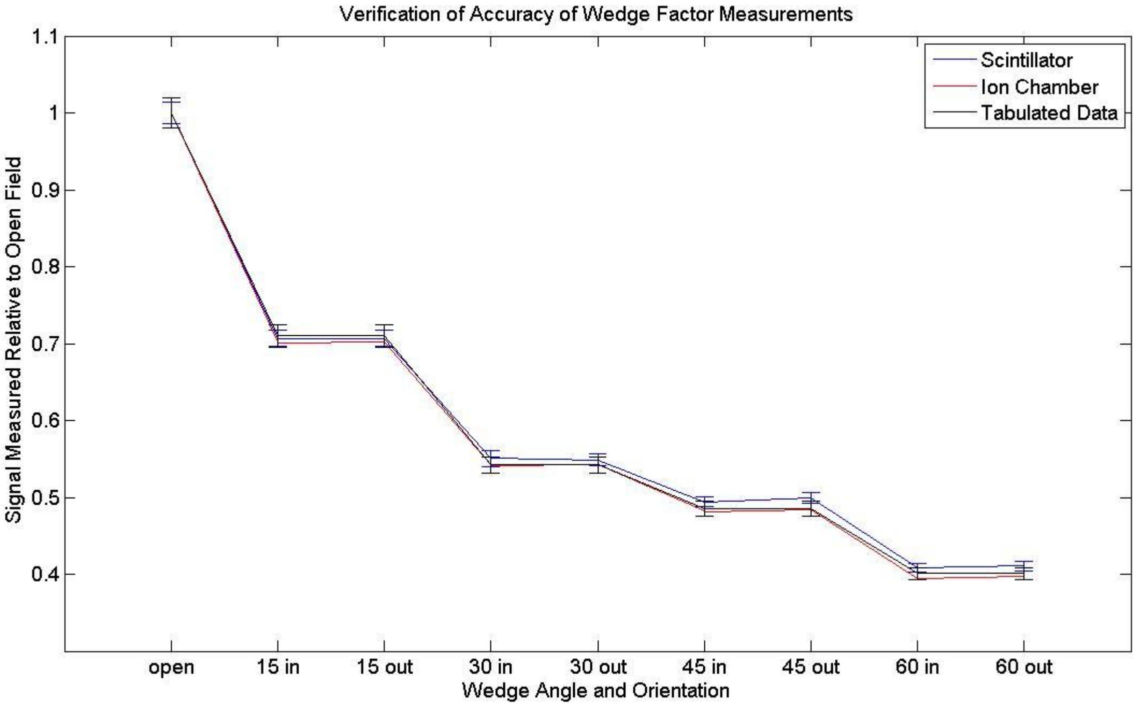

Figure 31: Measurement of physical wedge factors with scintillator and Protea detector, and local reference (clinical) data

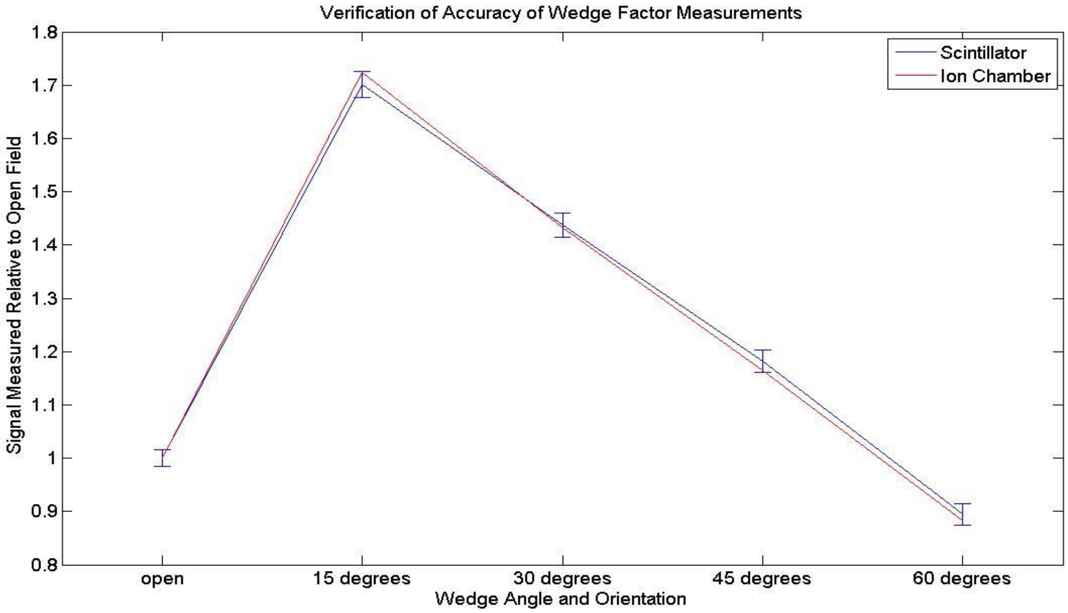

Figure 32: Verification of scintillation detector's ability to accurately measure enhanced dynamic wedge factors

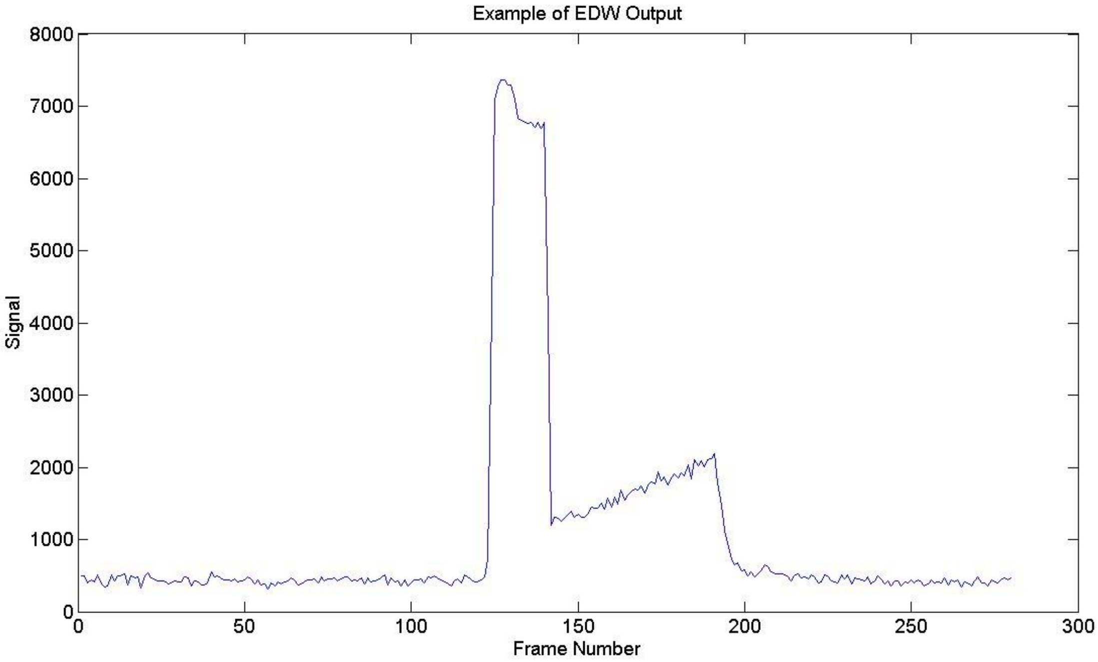

Figure 33: Depiction of signal measured during an enhanced dynamic wedge irradiation

The uncertainties in the normalized scintillator signals are much larger than those for the physical wedge factor measurements. The increased uncertainty occurs because the noise in the images was higher when performing the EDW measurements.

The output displayed in Figure 33 is interesting in that it clearly depicts the nature of the EDW treatment. The treatment begins with an open field and then the dose rate is dropped and slowly increased as the jaw is swept through the field.

Type of Field	Normalized Protea Signal	Normalized Scintillator Signal	Normalized Scintillator Signal Uncertainty
Open	1.00	1.00	0.02
15° EDW	1.72	1.70	0.02
30° EDW	1.43	1.44	0.02
45° EDW	1.16	1.18	0.02
60° EDW	0.88	0.89	0.02

Table 8: Measured normalized signals for enhanced dynamic wedge factors

4.4 Measurement of Relative Dose Factor

Compared to the other measurement sets presented, the error bars appear to be very large in this figure. The standard deviation of the measurements here range from 1.7% to 2.5%, which appears very large due to the fact that the range of values expected is much less in this measurement set. For example, the wedge factors have a range of 50-70% whereas the relative dose factor measurements only range by about 11%. That said, all of the Protea ion chamber and scintillation detector measurements agree to within the experimental uncertainty. This is a positive result, considering that this set of measurements is the one that would be the most adversely affected by the influence of Cerenkov radiation.

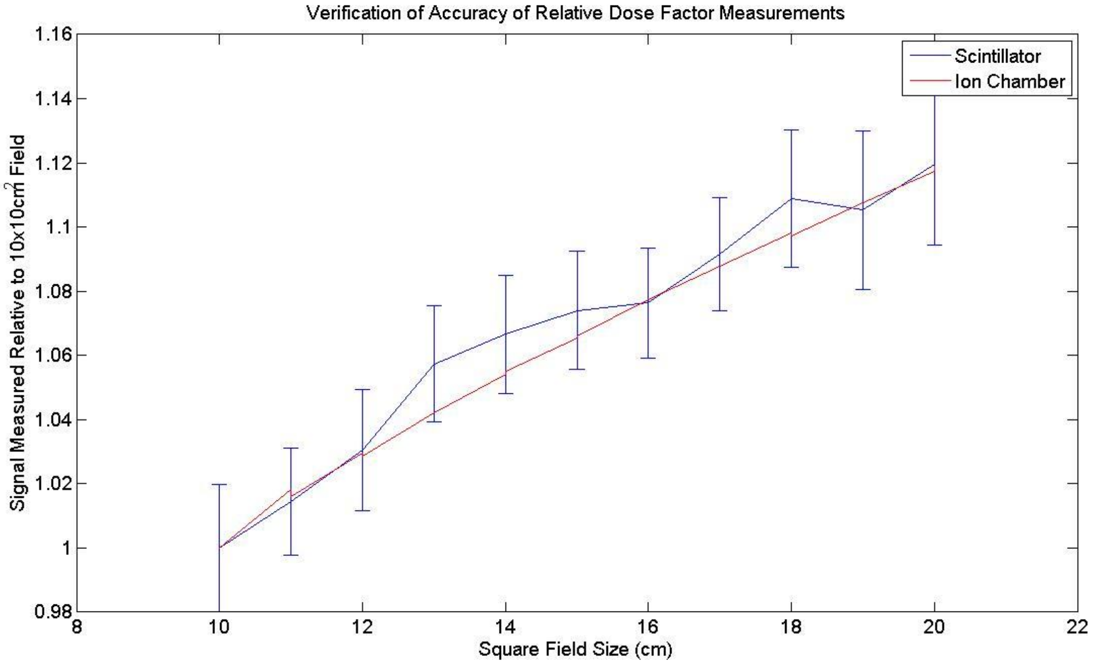

Figure 34: Measurement of relative dose factor with scintillation detector and ion chamber

As the field size gets to be 20x20 cm^2 or larger, a fairly significant portion of the detected signal is due to Cerenkov photons.

Figure 35 shows the signal measured from the reference fiber and evidences the strong increase in Cerenkov radiation as the field is increased. Whereas the actual increase in dose from 10x10 cm^2 to 20x20 cm^2 was measured to be 11.8%, the rise in Cerenkov radiation was measured to increase 236% over that same range of field sizes.

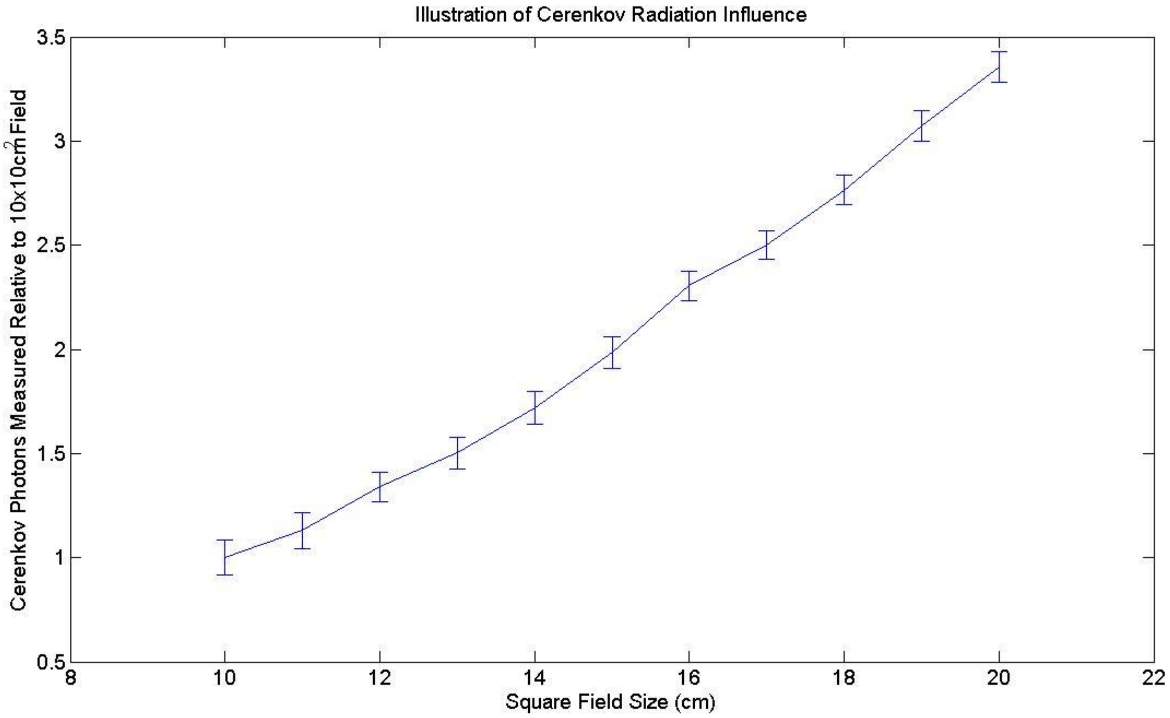

Figure 35: Cerenkov signal as a function of field size

It is also clear that the measured Cerenkov signal is a major contributor to the measurement uncertainty, having a mean standard deviation of just over 7.5%, compared to just under 2% for the scintillation signal. The 2% figure is also higher than it actually would be for the scintillation signal alone, since it was calculated after the Cerenkov signal was subtracted from the raw signal, and so the variation in Cerenkov signal is incorporated into the 2%.

4.5 Measurement of Tissue Maximum Ratio

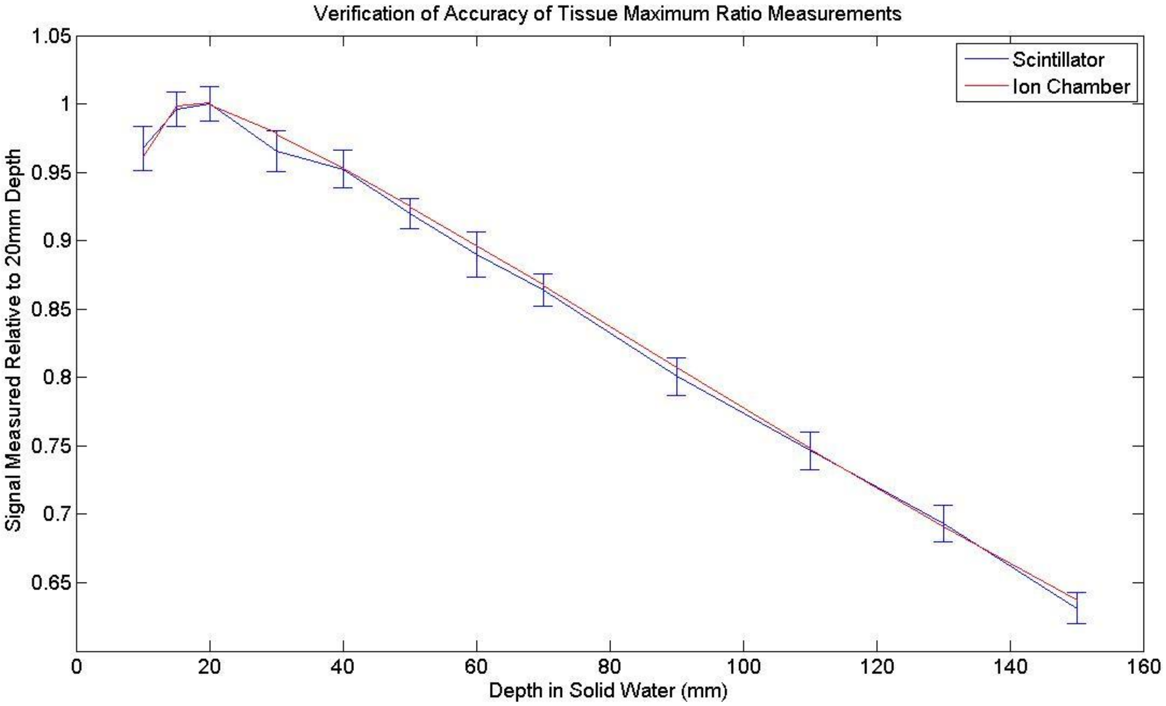

Figure 36: Plot of results of tissue maximum ratio measurements

Measurements were taken at 10, 15, 20, 30, 40, 50, 60, 70, 90, 110, 130 and 150 mm depths (see Figure 36). The measured signals were normalized to the signal measured at 20 mm depth, as this was the depth of maximum dose measured with both the scintillator and ion chamber. Clinically, d_{max} is taken to be 15 mm but the depth of maximum dose that was measured with both the scintillator detector and ion chamber was 20 mm. The raw protea signal measurements for 15 mm and 20 mm were 3.222, 3.221 3.228 and 3.225 respectively (two data points for each depth). The averaged doses over two data points only differ by 0.15% and so the discrepancy could be explained by setup error. Because the doses are so similar, the normalization point could have been chosen to be either 20 mm or 15 mm without a significant impact and 20 mm was ultimately chosen for internal consistency. It can be observed in the plot that all measurements agree well within uncertainty with the exception of the 30 mm depth, which does still agree within experimental uncertainty.

4.6 Measurement of IMRT Modulation Factor

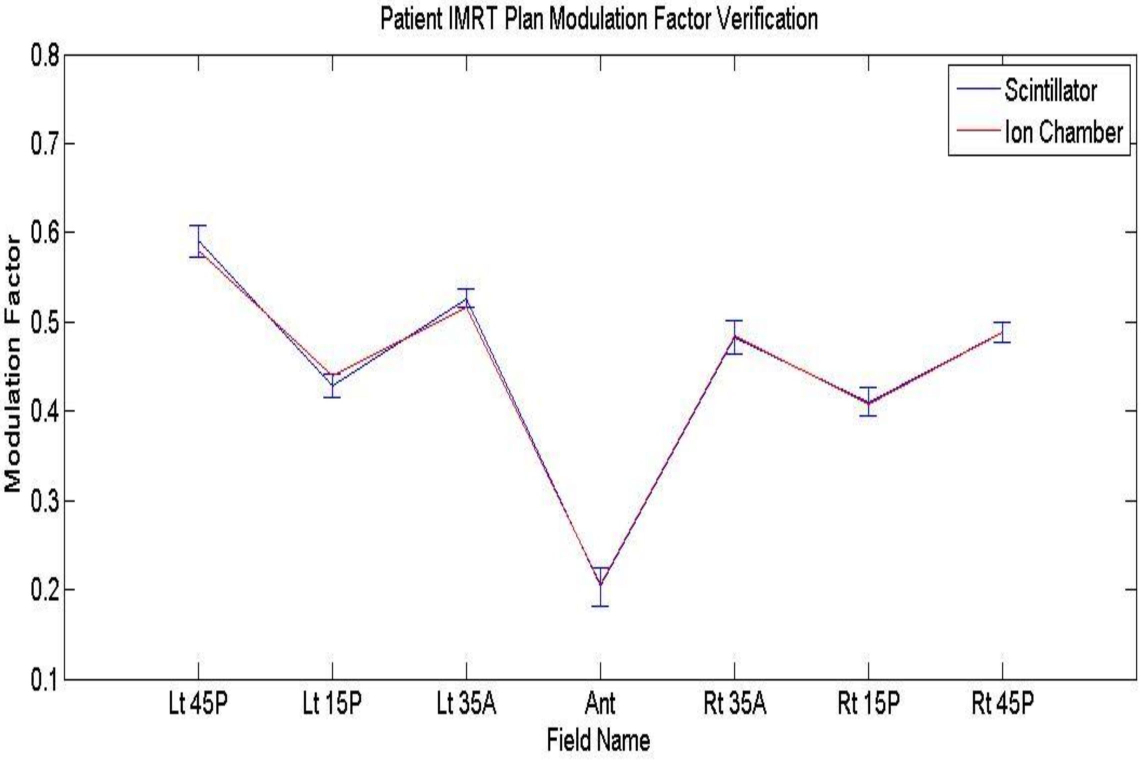

Figure 37: Measurement of IMRT modulation factor for patient's prostate IMRT plan

The uncertainties in the modulation factor were large in this set of measurements. The uncertainties were so large because the signals measured were often very small. Although one of the originally perceived benefits of using scintillators was that the high sensitivity would make the detector optimal for IMRT measurements, the instrumentation that is used is obviously limiting the detector's applicability due to the high uncertainties.

Field	Modulation Factor Measured by Protea	Modulation Factor Measured by Scintillator	Uncertainty in Modulation Factor Measured by Scintillator
Lt 45P	0.580	0.591	0.018
Lt 15P	0.440	0.428	0.014
Lt 35A	0.517	0.527	0.011
Ant	0.206	0.204	0.022
Rt 35A	0.485	0.483	0.018
Rt 15P	0.408	0.410	0.016
Rt 45P	0.489	0.488	0.011

Table 9: Results of measurements of IMRT modulation factor

Chapter 5: Discussion and Future Work

5.1 Discussion

The model for Betamax was simulated in EGSnrcMP and based on comparisons to known benchmarks, we are confident that the results are accurate. Based on this model, we were able to show that the scintillator is very radiologically water equivalent over a large energy range. The unrestricted stopping power ratio of water to Betamax differs by less than 3% in the energy range of 10 keV to 20 MeV, which gives a benefit over many other detector systems. For example, the scintillator can be used in larger volumes because the presence of the scintillator will not perturb the electron fluence as much as detectors that are less radiologically water equivalent would. The implication of this fact means that the scintillator could be used in an array or matrix of elements to obtain two or three dimensional dose distributions using a single treatment field.

By performing inverse square measurements, we were able to show that the scintillation output is independent of the dose rate. By varying the distance between the detector and the source of radiation, we were able to vary the dose rate from below 60% to above 120% of standard reference irradiation conditions. Throughout this entire range, the output of the scintillator matched both the expected theoretical output range as well as the output measured with the Protea detector to well within the measurement uncertainty. Although background information would tell us that we should expect the scintillator to be dose rate independent based on experience with plastic scintillators (Beddar, et al., 1992), we felt that it was important to verify this fact. The independence on dose rate was also verified with physical wedge factor measurements.

The scintillation detector was used to verify the transmission factors for four wedge angles in both the 'in' and 'out' configurations. The AAPM has determined that these transmission factors have to be measured on a monthly basis to ensure that the measured transmission factors agree with commissioning data (Klein, et al., 2009). This is important as it shows that the detector can suitably perform in the presence of dose gradients. Physical wedges are still used clinically and so this a clinically relevant experiment. Physical wedge measurements along the central axis are simple in as much as the dose rate doesn't change as a function of time and so the measured signal shape is similar to what would be measured for an open field. Wedge factor measurements can be quite susceptible to positioning errors since an error in detector placement along the wedge axis would mean that the beam can traverse more or less attenuator. Not only will this lead to a discrepancy in the measured transmission factor for a given field orientation, but additionally there will be an even larger discrepancy observed between complimentary orientations. Because these discrepancies were not observed, we are confident of chamber positioning and that we have an accurate sense of the location of the active measurement volume.

In addition to physical wedge transmission factors, the linac primary collimator jaws can be swept through the field to create a dose distribution similar to those observed using physical wedges. The AAPM recommends that transmission factors from these dynamic wedges be measured monthly for either 45° or 60°. The wedge factors were measured for wedge angles of 15°, 30°, 45° and 60° and the measured wedge factors all agreed with the wedge factors measured by a Protea ion chamber. Compared to irradiations using a physical wedge, this is a relatively complex situation, since the dose rate varies with time. The dose rate varies in time due to two factors: first, the radiation dose delivery rate is not constant throughout the treatment and additionally the field size is also varied.

Variation in pulse repetition rate is not a problem in general, but can become a complication if the signal measured becomes low with respect to background. This becomes troubling since it can become difficult for the user to differentiate between successive irradiations . Furthermore, the selection of cutoff threshold that determines if a frame corresponds to a 'beam on' time or a 'beam off' time becomes problematic. Throughout our measurements the signal did not ever drop low enough for either of the two preceding concerns to be relevant, at least for the signal fiber.

When we instead look at the Cerenkov fiber, we see that there are times when the Cerenkov signal level drops low enough to be comparable to the background.

In Figure 38 it is apparent that the around frame number 150 the signal drops low enough so that the measured signal isn't much higher than background. This presents a challenging situation, as it becomes difficult or the user to select a cutoff to differentiate signal and background. This is a challenge that can be avoided by two ways: one can either increase the measured signal or decrease the background.

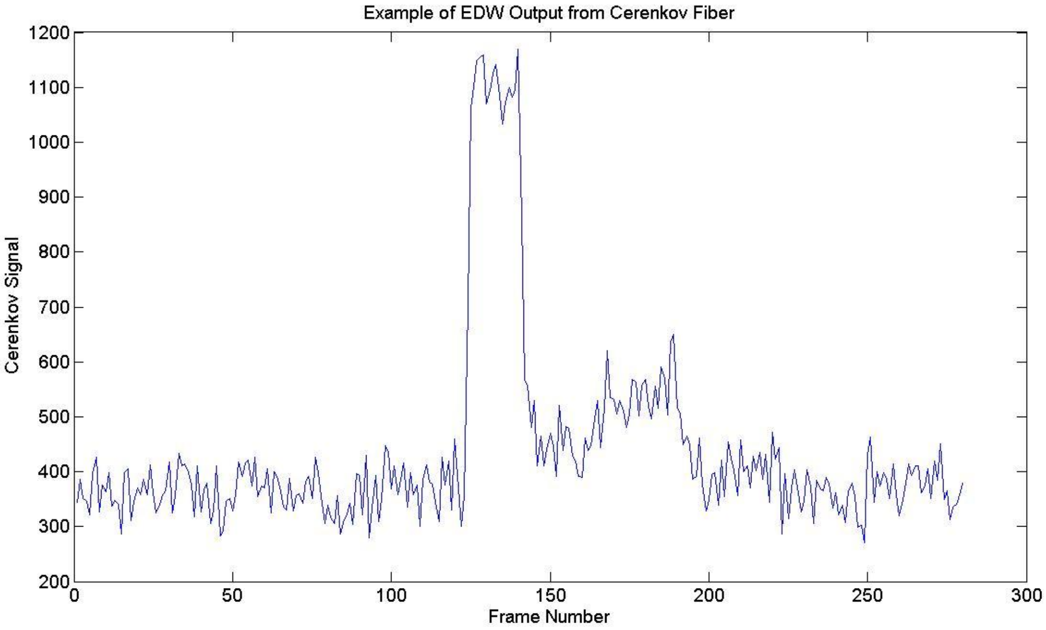

Figure 38: Signal measured due to Cerenkov photons during EDW measurement

It is hardly advantageous to increase the Cerenkov signal unless the signal from the scintillator is also increasing. To increase the signal, we would need to explore a better coupling mechanism between the fibers and the CCD face. In general, fiber optic interfaces need to be treated very carefully to obtain high coupling coefficients. To facilitate this, commercial products are available that allow for polishing of the fiber optic ends. The cost of these products is large with respect to the other costs associated with the project and so it was decided that the products would not be employed. Furthermore, the local staff does not have the training or experience to be able to operate these specialized devices. To decrease the image noise and background we would have to either introduce a cooling mechanism to the current CCD or move to another CCD entirely. The current CCD was specifically chosen due to the fact that it had excellent noise characteristics for a standard CCD used in webcams, but scientific-grade CCDs offer much better noise characteristics. We investigated cooling earlier using a Peltier cell, but the cooling appeared to be erratic, leading to variations in the background signal that would be very difficult to account for.

As with the previously discussed results, every scintillator measurement point of the relative dose factor verification agreed with the ion chamber measurements to within experimental uncertainty. This measurement set involved many fields that were relatively large, which introduced complications. As the field size was increased, a substantial amount of Cerenkov radiation was produced and so the importance of Cerenkov subtraction was paramount. Unfortunately, the Cerenkov signal is very noisy and therefore subtracting the Cerenkov signal from the scintillator signal injects significant variability in the measured signal. This would again support the suggestion that the amount of signal needs to be increased or the amount of noise needs to be decreased by one means or another.

The tissue maximum ratio measurements also provided good results with the exception of the 30 mm solid water depth, where the ion chamber and scintillator measurements still agreed within experimental uncertainty. We believe that a plausible reason for the discrepancy would be that the setup shifted when the 30 mm measurement was taken.

The IMRT modulation factor measurements showed that the scintillation detector and ion chamber predict the same factor to within the uncertainty of the experiment. This is a positive result, as IMRT treatments use small fields with high gradients, which can be difficult for some detectors to measure properly (Frelin, et al., 2008). The small fields proved to be both a positive and negative contributor regarding the influence of Cerenkov radiation: smaller fields produce smaller quantities of Cerenkov radiation, but the Cerenkov removal technique that we employ begins to be less effective. The dual parallel fiber subtraction method is valid under the assumption that both fibers receive the same radiation fluence. In IMRT fields this assumption starts to break down, as steep gradients can cause a difference in fluence to be observed. This is the primary drawback of the duplex fiber Cerenkov subtraction method and other methods of Cerenkov subtraction would be better suited for this application. Furthermore, the small fields used can lead to low Cerenkov signals with respect to background leading to high uncertainties.

In general, the detector has performed well. The detector was shown to be dose rate independent, and was able to correctly measure physical wedge factors, enhanced dynamic wedge factors, relative dose factors, tissue maximum ratios as well as the modulation factors for a patient's IMRT plan. The main factor that prevents this detector from obtaining better results is the high noise and background levels. In the most basic of terms, it is felt that this could be ameliorated by either increasing the measured signal or decreasing the noise and background.

One possibility to decrease the background would be to move to a glass fiber optic cable with a much smaller core. The diameter of the plastic cable that was used was nominally 1 mm, whereas glass-core optical fibers are produced that have diameters on the order of tens of microns. We briefly experimented with a 62.5 micron Infinicor cable (Corning, NY) but found it difficult to measure a signal through the fiber. This was most likely due to the difficulty in making contact between the CCD and the much smaller fiber optic. The optical fiber was wrapped in Teflon fibers for structural support, which meant that air gaps existed between the fiber optic and the external jacket. Using this system would require a complete redesign of the scintillation detector chamber, since the current design uses the fiber optic cable itself to seal the liquid into the chamber.

As was discussed earlier, the common way to decrease background and thermal noise in a CCD is to introduce cooling. The thermal noise increases substantially with increased temperature and so it is important to keep temperatures low (Widenhorn, et al., 2002). Not only do temperatures need to be low, but they also need to be almost constant so that the CCD output doesn't change during measurements. When we experimented with using a Peltier cell, the temperature varied too much to be able to be used without the introduction of temperature sensors that would be able to control the cooling by controlling the temperature to within a small temperature range. Although, in general, this could be done, it was felt that introducing this circuitry is beyond the scope of the project and doesn't fit with the original intentions, which was to employ a simple apparatus to investigate the dosimetry potential of this fluid.

Given the issues that have been encountered with high noise and background levels, one might be tempted to suggest the use of photodiodes instead of a CCD. Mounted photodiodes can be purchased with a relatively low cost (on the order of $100) meaning that they are still relatively inexpensive (yet still more than the current setup). Having obtained a photodiode, one could then mount the fiber optic to the photodiode in a similar fashion to what we did with the CCD and then use a coaxial cable to measure the output with an electrometer. I believe this would be an appropriate tool to measure point doses, but comes with its own set of drawbacks.

- Photodiodes are a single-element detector, meaning that Cerenkov subtraction would require either using a different subtraction method or multiple photodiodes. Using multiple photodiodes would require additional electronics that can increase the complexity. Other subtraction methods require spectral discrimination and this in not measurable with photodiodes.
- One of the main benefits to using liquid scintillators was the ability to easily create multiple detector element phantoms. To be able to accommodate this, photodiode arrays would be required, which would increase the cost and complexity.

5.2 Future Work

To expand on this work, one would need to investigate the aforementioned methods for increasing the signal or decreasing the background and thermal noise. We feel that the coupling efficiency between the fiber optic and the detector could be greatly improved by using specialized polishing equipment. Furthermore, the inexpensive, commercial webcam CCD that was used would need to be replaced to make the detector system clinically viable. This could be done in a number of ways, including using photodiodes, scientific CCDs or a scientific CMOS detector. Any of these detectors would offer superior noise characteristics to the CCD that we employed.

It would also be beneficial to use a single, long duplex optical fiber to take the CCD out of the treatment vault instead of using USB extenders. When we performed the experiments we had multiple USB cables and it became problematic to manage as they could become disconnected if the user was not careful. If this was done during an acquisition, even during previews, the computer system would crash. Having a single duplex fiber optic cable would also be beneficial because the losses in a glass core fiber optic cable are much lower. The attenuation in the USB cable was approximately 0.42% per meter (ignoring junctions), whereas the loss in a Corning 62.5 μm cable would be less than 0.0067% per meter at 850nm. using a single, long cable would also allow us to bring the CCD outside of the room, which would alleviate the need to shield the CCD. This would both reduce the cost as well as make the detector system more easily portable.

One of the major benefits in using a liquid scintillator is the fact that it will conform to the volume of any container it is poured into. This could have large benefits when considering a two dimensional array of detector elements or even a three dimensional volume. Although these concepts were not explored in this work, they should be achievable with the appropriate hardware. For example, if someone were to use a pair scientific CMOS or CCD detectors, it is conceivable to produce a three dimensional dose distribution from a large volume sample of Betamax in a sequence of several short acquisitions.

5.3 Conclusion

The goal of this work was to investigate the dosimetric properties of a scintillating liquid through calculation, simulation and measurement. To the latter end, we examined the possibility of combining a standard webcam CCD with Betamax liquid scintillation cocktail for use in megavoltage external beam radiotherapy. The detector was able to accurately reproduce a variety of dosimetric quantities, such as the linear accelerators relative dose factor, the tissue maximum ratio, physical and enhanced dynamic wedge factors as well as IMRT modulation factors.

The detector system that was used is unsuitable for clinical use due to a low signal levels, high noise levels and high background signal. Multiple ways of increasing the signal and reducing noise and background have been discussed that could greatly increase the ability to use this detector system in a clinical setting.

The hardware system itself was not the focus of the project, though, as our primary focus was to determine the feasibility of using the Betamax liquid scintillation cocktail for external beam dosimetry. The Monte Carlo simulations and the measurements that were performed confirm that Betamax is a suitable candidate for external beam dosimetry and further investigation with it is warranted.

Bibliography

Archambault, L. et al., 2006. Measurement accuracy and Cerenkov removal or high performance, high spatial resolution scintillation dosimetry. *Medical Physics.*

Beddar, A. S., 2007. Plastic scintillation dosimetry and its application to radiotherapy. *Radiation Measurements,* pp. S124-S133.

Beddar, A. S., Mackie, T. R. & Attix, F. H., 1992. Water-equivalent plastic scintillation detectors for high energy beam dosimetry: I. Physical characteristics and theoretical considerations. *Physics in Medicine and Biology,* pp. 1883-1900.

Beddar, A. S., Mackie, T. R. & Attix, F. X., 1992. Water-equivalent plastic scintillation detectors for high-energy beam dosimetry: II. Properties and emasurements. *Physics in Medicine and Biology,* pp. 1901-1913.

Beddar, S. et al., 2009. Exploration of the potential of liquid scintlilators for real-time 3D dosimetry of intensity modulated proton beams. *Medical Physics,* pp. 1736-1743.

Birks, J. B., 1964. *The Theory and Practice of Scintillation Counting.* s.l.:Pergamon Press.

Bortfeld, T., 2006. IMRT: a review and preview. *Physics in Medicine and Biology,* pp. 363-379.

Carlson, 1975. *Photoelectron and Auger Spectroscopy.* New York and London: Plenum Press.

Carol, M. et al., 1996. Initial Clinical Experience with the Peacock Intensity Modulation of a 3-D Conformal Radiation Therapy System. *Stereotactic and Functional Neurosurgery.*

Cerenkov, P. A., 1937. Visible Radiation Produced by Electrons Moving in a Medium with Velocities Exceeding that of Light. *Phys. Rev.*.

Charman, W. N., 1952. Cosmic Rays and Image Intensifier Dark Current. *Advances in Electronics and Elecron Physics,* pp. 705-712.

Clift, M. A., Johnston, P. N. & Webb, D. V., 2002. A temporal method of avoiding the Cerenkov. *Physics in Medicine and Biology,* pp. 1421-1434.

Clift, M. A., Sutton, R. A. & Webb, D. V., 2000. Dealing with Cerenkov radiation generated in organic scintillator dosimeters by bremsstrahlung beams. *Physics in Medicine and Biology,* pp. 1165-1182.

Convery, D. J. & Rosenbloom, M. E., 1992. The generation of intensity-modulated fields for conformal radiotherapy by dynamic collimation. *Physics in Medicine and Biology,* pp. 1359-1374.

Dai, X. et al., 2008. Wavelength shifters for water Cherenkov detectors. *Nuclear Instruments and Methods in Physics Research A,* pp. 290-295.

Digi-Key, n.d. *http://www.digikey.ca/product-detail/en/GHCP4002/FB141-1-ND/295768.* [Online]
[Accessed 8 June 2012].

Dyer, A., 1980. *Liquid Scintillation Counting Practice.* London: Heyden.

Frelin, A.-M.et al., 2008. The DosiMap, a new 2D scintillating dosimeter for IMRT quality assurance: Characterization of two Cerenkov discrimination methods. *Medical Physics,* pp. 1651-1662.

Golovkin, S. V. et al., 1995. Radiation damage studies on new liquid scintillators and liquid-core scintillating fibers. *Nuclear Instruments & Methods in Physics Research Section A,* pp. 283-291.

Hamada, M. M., Rela, P. R., da Costa, F. E. & de Mesquita, C. H., 1999. Radiation damage studies on the optical and mechanical properties of plastic scintillators. *Nuclear Instruments and Methods in Physics Research A,* pp. 148-154.

Howard, P. L., 1976. *Basic Liquid Scintillation Counting.* Chicago: American Society of Clinical Pathologists.

Howell, S. B., 2000. *Handbook of CCD Astronomy.* Cambridge: Cambridge University Press.

Janesick, J. R., 2001. *Scientific Charge-Coupled Devices.* s.l.:SPIE Press.

Jelley, J. V., 1958. *Cerenkov Radiation and its Applications.* New York: Pergamon Press.

Johns, H. E. & Cunningham, J. R., n.d. *The Physics of Radiology, Fourth Edition.*

Khan, 1994. *The Physics of Radiation Therapy Second Ediion.* Baltimore: William & Wilkins.

Klein, E. E. et al., 2009. Task Group 142 report: Quality assurance of medical accelerators. *Medical Physics.*

Knoll, G. F., 2010. *Radiation Detection and Measurement.* s.l.:John Wiley and Sons.

Lacroix, F. et al., 2008. Clinical prototype of a plastic water-equivalent scintillating fiber dosimeter array for QA applications. *Medical Physics,* pp. 3682-3690.

Leavitt, D., Martin, M., Moeller, J. & Lee, W. L., 1990. Dynamic wedge field techniques through computer-controlled collimator motion and dose delivery. *Medical Physics* .

Lecoq, P., Annenkov, A., Gektin, A. & Korzhik, M., 2006. *Inorganic Scintillators for Detector Systems: Physical Principles and Crystal Engineering.* s.l.:Springer.

Liu, C., Li, Z. & Palta, J., 1998. Characterizing output for the Varian enhanced dynamic wedge field. *Medical Physics* .

Magnan, P., 2003. Detection of visible photons in CCD and CMOS: A comparative review. *Nuclear Instruments and Methods in Physics Research A,* pp. 199-212.

Martinez, P. & Klotz, A., 1998. *A Practical Guide to CCD Astronomy.* Cambridge: Cambridge University Press.

Ponisch, F. et al., 2009. Liquid Scintillator for 2D dosimetry for high-energy photon beams. *Medical Physics,* pp. 1478-1485.

Rice, P. K., Hansen, J. L., Svensson, G. K. & Siddon, R. L., 1987. Measurements of dose distributions in small beams of 6MV x-rays. *Phys. Med. Biol.,* pp. 1087-1099.

Robinson, D., 2008. Inhomogeneity correction and the analytic anisotropic algorithm. *Journal of Applied Clinical Medical Physics.*

Tailor, R. C., Hanson, W. F., Wells, N. & Ibbott, G. S., 2006. Consistency of absorbed dose to water measurements. *Medical Physics,* pp. 18188-1828.

Taylor, J. R., 1997. *An Introduction to Error Analysis.* s.l.:University Science Books.

Tipler, P. A. & LLewellyn, R. A., 2002. *Modern Physics Fourth Edition.* s.l.:W.H Freeman.

Walker, G., 1987. *Astronomical Observations.* Cambridge: Camb University Press.

Widenhorn, R. et al., 2002. Temperature dependence of dark current in a CCD. *Proceedings of SPIE,* Volume 2669.

Yu, C. X., 1995. Intensity-modulated arc therapy with dynamic multileaf. *Physics in Medicine and Biology,* pp. 1435-1449.

Zhu, R.-y., 1998. Radiation damage in scintillating crystals. *Nuclear Instruments and Methods in Physics Research A,* pp. 297-311.

Appendix: Calculating Experimental Uncertainty

The statistical uncertainty in a given set of measurements was taken to be the standard deviation of the set. For example, most scintillator measurements were taken twelve times under the exact same set of conditions and then the standard deviation of the signal values in the set were computed and used as the uncertainty.

Because of the necessity to perform Cerenkov subtraction, the uncertainties from both the scintillation signal and the Cerenkov signal have to be added. Let us denote the uncertainty in the scintillator signal σ_{scint}, the uncertainty in the Cerenkov signal σ_{Cerenkov} and the resultant uncertainty σ_{signal}. To compute the resulting uncertainty, we need to use the following equation (Taylor, 1997):

$$\sigma_{signal} = \sqrt{\sigma_{scint}^2 + \sigma_{cerenkov}^2} \tag{21}$$

Generally, the data is presented in comparison to a reference condition, for example, in the case of wedge factors, the wedge factor is given as the signal measured during the treatment field divided by the signal measured for an open field. If we were to want to find the uncertainty in this quotient, we would have to use the following equation:

$$\sigma_{quotient} = S_{quotient} \cdot \sqrt{\left(\frac{\sigma_{treatment}}{S_{treatment}}\right)^2 + \left(\frac{\sigma_{reference}}{S_{reference}}\right)^2} \tag{22}$$

In equation 22, the S terms refer to the signal values. In this case, we are adding fractional uncertainties in quadrature.